1 **The Education and Research 3D Radiative Transfer Toolbox (EaR³T) – Towards the**

2 **Mitigation of 3D Bias in Airborne and Spaceborne Passive Imagery Cloud Retrievals**

3

4 Hong Chen[1,2], K. Sebastian Schmidt[1,2], Steven T. Massie[2], Vikas Nataraja[2], Matthew S. Norgren[2],

5 Jake J. Gristey[3,4], Graham Feingold[4], Robert E. Holz[5], Hironobu Iwabuchi[6]

6

7

8 [1]Department of Atmospheric and Oceanic Sciences, University of Colorado, Boulder, CO, USA

9 [2]Laboratory for Atmospheric and Space Physics, University of Colorado, Boulder, CO, USA

10 [3]Cooperative Institute for Research in Environmental Sciences, University of Colorado,

11 Boulder, CO, USA

12 [4]NOAA Chemical Sciences Laboratory, Boulder, CO, USA

13 [5]Space Science and Engineering Center, University of Wisconsin–Madison, Madison, WI, USA

14 [6]Center for Atmospheric and Oceanic Studies, Tohoku University, Sendai, Miyagi, Japan

15

16

17

18

19 *Correspondence to*: Hong Chen (hong.chen-1@colorado.edu)

Abstract

We introduce the Education and Research 3D Radiative Transfer Toolbox (EaR³T, pronounced [ɜːt]) for quantifying and mitigating artifacts in atmospheric radiation science algorithms due to spatially inhomogeneous clouds and surfaces, and show the benefits of automated, realistic radiance and irradiance generation along extended satellite orbits, flight tracks from entire aircraft field missions, and synthetic data generation from model data. EaR³T is a modularized Python package that provides high-level interfaces to automate the process of 3D radiative transfer (RT) calculations. After introducing the package, we present initial findings from four applications, which are intended as blueprints to future in-depth scientific studies. The first two applications use EaR³T as a satellite radiance simulator for the NASA Orbiting Carbon Observatory 2 (OCO-2) and Moderate Resolution Imaging Spectroradiometer (MODIS) missions, which generate synthetic satellite observations with 3D-RT on the basis of cloud field properties from imagery-based retrievals and other input data. In the case of inhomogeneous cloud fields, we show that the synthetic radiances are often inconsistent with the original radiance measurements. This lack of radiance consistency points to biases in heritage imagery cloud retrievals due to sub-pixel resolution clouds and 3D-RT effects. They come to light because the simulator's 3D-RT engine replicates processes in nature that conventional 1D-RT retrievals do not capture. We argue that 3D radiance consistency (closure) can serve as a metric for assessing the performance of a cloud retrieval in presence of spatial cloud inhomogeneity even with limited independent validation data. The other two applications show how airborne measured irradiance data can be used to independently validate imagery-derived cloud products via radiative closure in irradiance. This is accomplished by simulating downwelling irradiance from geostationary cloud retrievals of Advanced Himawari Imager (AHI) along all the below-cloud aircraft flight tracks of the Cloud, Aerosol and Monsoon Processes Philippines Experiment (CAMP²Ex, NASA 2019), and comparing the irradiances with the collocated airborne measurements. In contrast to case studies in the past, EaR³T facilitates the use of observations from entire field campaigns for the statistical validation of satellite-derived irradiance. From the CAMP²Ex mission, we find a low bias of 10% in the satellite-derived cloud transmittance, which we are able to attribute to a combination of the coarse resolution of the geostationary imager and 3D-RT biases. Finally, we apply a recently developed context-aware Convolutional Neural Network (CNN) cloud retrieval framework to high-resolution airborne imagery from CAMP²Ex and show that the retrieved cloud optical thickness fields lead to better 3D radiance consistency than the heritage independent pixel algorithm, opening the door to future mitigation of 3D-RT cloud retrieval biases.

1. Introduction

Three-dimensional cloud effects in imagery-derived cloud properties have long been considered an unavoidable error source when estimating the radiative effect of clouds and aerosols. Consequently, research efforts involving satellite, aircraft, and surface observations in conjunction with modeled clouds and radiative transfer calculations have focused on systematic bias quantification under different atmospheric conditions. Barker and Liu (1995) studied the so-called independent pixel approximation (IPA) bias in cloud optical thickness (COT) retrievals from shortwave cloud reflectance. The bias arises when approximating the radiative transfer relating to COT and measured reflectance at the pixel or cloud column level through one-dimensional (1D) radiative transfer (RT) calculations, while ignoring its radiative context. However, net horizontal photon transport and other effects such as shading engender column-to-column radiative interactions that can only be captured in a three-dimensional (3D) framework, and can be regarded as a 3D perturbation or bias relative to the 1D-RT (IPA) baseline. 3D biases affect not only cloud remote sensing but they also propagate into the derived irradiance fields and cloud radiative effects (CRE). Since the derivation of regional and global CRE relies heavily on satellite imagery, any systematic 3D bias impacts the accuracy of the Earth's radiative budget. Likewise, imagery-based aerosol remote sensing in the vicinity of clouds can be biased by net horizontal photon transport (Marshak et al., 2008). Additionally, satellite shortwave spectroscopy retrievals of CO_2 mixing ratio are affected by nearby clouds (Massie et al., 2017), albeit through a different physical mechanism than in aerosol and cloud remote sensing (Chen et al., 2023).

Given the importance of 3D perturbations for atmospheric remote sensing, ongoing research seeks to mitigate the 3D effects. Cloud tomography, for example, inverts multi-angle radiances to infer the 3D cloud extinction distribution (Levis et al., 2020). This is achieved through iterative adjustments to the cloud field until the calculated radiances match the observations. Convolutional neural networks (CNNs, Masuda et al., 2019; Nataraja et al., 2022) account for 3D-RT perturbations in COT retrievals through pattern-based machine learning that operates on collections of imagery pixels, rather than treating them in isolation like IPA. Unlike tomography, CNNs require training based on extensive cloud-type specific synthetic data with the ground truth of cloud optical properties and their associated radiances from 3D-RT calculations. Once the CNNs are trained, they do not require real-time 3D-RT calculations and can therefore be useful in an operational setting. Whatever the future may hold for context-aware multi-pixel or multi-sensor

82   cloud retrievals, there is a paradigm shift on the horizon that started when the radiation concept

83   for the Earth Clouds, Aerosol and Radiation Explorer (EarthCARE, Illingworth et al., 2015) was

84   first proposed (Barker et al., 2012). It foresees a closure loop where broadband radiances, along

85   with irradiance, are calculated in a 3D-RT framework from multi-sensor input fields (Barker et al.,

86   2011), and subsequently compared to independent observations by radiometers pointing in three

87   directions (nadir, forward-, and backward-viewing along the orbit). This built-in radiance closure

88   can serve as an accuracy metric for any downstream radiation products such as heating rates and

89   CRE. Any inconsistencies can be used to nudge the input fields towards the truth in subsequent

90   loop iterations akin to optimal estimation, or propagated into uncertainties of the cloud and

91   radiation products.

92   This general approach to radiative closure is also being considered for the National

93   Aeronautics and Space Administration (NASA) Atmospheric Observation System (AOS,

94   developed under the A-CCP, Aerosol and Cloud, Convection and Precipitation study), a mission

95   that is currently in its early implementation stages. Owing to its focus on studying

96   aerosol-cloud-precipitation-radiation interactions at the process level, it requires radiation

97   observables at a finer spatial resolution than achieved with missions to date. At target scales close

98   to 1 km, 3D-RT effects are much more pronounced than at the traditional 20 km scale of NASA

99   radiation products (O'Hirok and Gautier, 2005; Ham et al., 2014; Song et al., 2016; Gristey et al.,

100   2020a). Since this leads to biases beyond the desired accuracy of the radiation products, mitigation

101   of 3D-RT cloud remote sensing biases needs to be actively pursued over the next few years.

102   Transitioning to an explicit treatment of 3D-RT in operational approaches entails a new

103   generation of code architectures that can be easily configured for various instrument constellations,

104   interlink remote sensing parameters with irradiances, heating rates, and other radiative effects, and

105   can be used for automated processing of large data quantities. A number of 3D solvers are available

106   for different purposes, for example, the I3RC (International Intercomparison of 3D Radiation

107   Codes: Cahalan et al., 2005) community Monte Carlo code[1], which now also includes an online

108   simulator[2] that was described in Várnai et al. (2022) and used in Gatebe et al. (2021); MCARaTS

109   (Monte Carlo Atmospheric Radiative Transfer Simulator[3]: Iwabuchi, 2006); MYSTIC (Monte

---

[1] https://earth.gsfc.nasa.gov/climate/model/i3rc, last accessed on 26 November, 2022.
[2] http://i3rcsimulator.umbc.edu, last accessed on 26 November, 2022.
[3] https://sites.google.com/site/mcarats/monte-carlo-atmospheric-radiative-transfer-simulator-mcarats, last accessed on 26 November, 2022.

110 Carlo code for the physically correct tracing of photons in cloudy atmospheres: Mayer, 2009),
111 which is embedded in libRadtran (library for radiative transfer, Mayer and Kylling, 2005);
112 McSCIA (Monte Carlo [RT] for SCIAmachy: Spada et al., 2006), which is optimized for satellite
113 radiance simulations (including limb-viewing) in a spherical atmosphere; McARTIM
114 (Deutschmann et al., 2011), with several hyperspectral polarimetric applications such as
115 differential optical absorption spectroscopy; and SHDOM (Spherical Harmonic Discrete Ordinate
116 Method[4]: Evans, 1998), which, unlike the other methods, is a deterministic solver with polarimetric
117 capabilities (Doicu et al., 2013; Emde et al., 2015) that is differentiable and can therefore be used
118 for tomography (Loveridge et al., 2022).

119   For the future operational application of 3D-RT, it is, however, desirable to run various
120 different solvers in one common architecture that automates the processing of various formats of
121 3D atmospheric input fields (including satellite data), allows the user to choose from various
122 options for atmospheric absorption and scattering, and simulates radiance and irradiance data for
123 real-world scenes. Here, we introduce one such tool that could serve as the seed for this architecture:
124 the Education and Research 3D Radiative Transfer Toolbox (EaR³T, pronounced [ɜːt]). It has been
125 developed over the past few years at the University of Colorado to automate 3D-RT calculations
126 based on imagery or model cloud fields. It can be operated in two ways– 1) with minimal user
127 input, where certain RT parameters are bypassed through default settings, for quick radiation
128 conceptual analysis; 2) with detailed RT parameters setup by user for radiation closure purpose.
129 EaR³T is maintained and extended by graduate students as part of their education, and applied to
130 various different research projects including machine learning for atmospheric radiation and
131 remote sensing (Gristey et al., 2020b; 2022; Nataraja et al., 2022), as well as radiative closure and
132 satellite simulators (this paper and Chen et al., 2023). It is implemented as a modularized Python
133 package with various application codes that combine the functionality in different ways, which,
134 once set up, autonomously process large amounts of data required by airborne and satellite remote
135 sensing and for machine learning applications.

136   The goal of the paper is to introduce EaR³T as a versatile tool for systematically quantifying
137 and mitigating 3D cloud effects in radiation science as foreseen in future missions. To do so, we
138 will first showcase EaR³T as an automated radiance simulator for two satellite instruments, the
139 Orbiting Carbon Observatory-2 (OCO-2, application code 1, App. 1) and the Moderate Resolution

---

[4] https://coloradolinux.com/shdom, last accessed on 26 November, 2022.

Imaging Spectroradiometer (MODIS, application code 2, App. 2) from publicly available satellite retrieval products. In the spirit of radiance closure, the intended use is the comparison of modeled radiances with the original measurements to assess the accuracy of the input data, as follows: operational IPA COT products are made using 1D-RT, and thus the accompanying radiances are consistent with the original measurements under that 1D-RT assumption only. That is, self-consistency is assured if 1D-RT is used in both the inversion and radiance simulation. However, since nature creates 3D-RT radiation fields, we break this traditional symmetry in this manuscript and introduce the concept of 3D radiance consistency where closure is only achieved if the original measurements are consistent with the 3D-RT (rather than the 1D-RT) simulations. The level of inconsistency is then used as a metric for the magnitude of 3D-RT retrieval artifacts as envisioned by the architects of the EarthCARE radiation concept (Barker et al., 2012).

Subsequently, we discuss applications where EaR^{3}T performs radiative closure in the traditional sense, i.e., between irradiances derived from satellite products and collocated airborne or ground-based observations. The aircraft Cloud, Aerosol and Monsoon Processes Philippines Experiment (CAMP^{2}Ex, Reid et al., 2023), conducted by NASA in the Philippines in 2019, serves as a testbed of this approach. Here, we use EaR^{3}T's automated processing capabilities to derive irradiance from geostationary imagery cloud products and then compare these to cumulative measurements made along all flight legs of the campaign (application code 3, App. 3). In contrast to previous studies that often rely on a number of cases (e.g., Schmidt et al., 2010; Kindel et al., 2010), we perform closure systematically for the entire data set, enabling us to identify 3D-RT biases in a statistically significant manner. Finally, we apply a regionally and cloud type specific CNN, introduced by Nataraja et al. (2022) that is included with the EaR^{3}T distribution, to high-resolution camera imagery from CAMP^{2}Ex. This last example demonstrates mitigation of 3D-RT biases in cloud retrievals using the concept of radiance closure to quantify its performance against the baseline IPA (application code 4, App. 4).

The general concept of EaR^{3}T with an overview of the applications, along with the data used for both parts of the paper is presented in section 2, followed by a description of the procedures of EaR^{3}T in section 3. Results for the OCO-2 and MODIS satellite simulators (part 1) are shown in section 4, followed by the quantification and mitigation of 3D-RT biases with CAMP^{2}Ex data in section 5 and section 6 (part 2). A summary and conclusion are provided in

170   section 7. The code, along with the applications presented in this paper, can be downloaded from

171   the GitHub repository: https://github.com/hong-chen/er3t.

172

173   **2. Functionality and Data Flow within EaR³T**

174   **2.1 Overview**

175   To introduce EaR³T as a satellite radiance simulator tool and to demonstrate its use for the

176   quantification and mitigation of 3D cloud remote sensing biases, five applications (Figure 1) are

177   included in the GitHub software release:

178

179
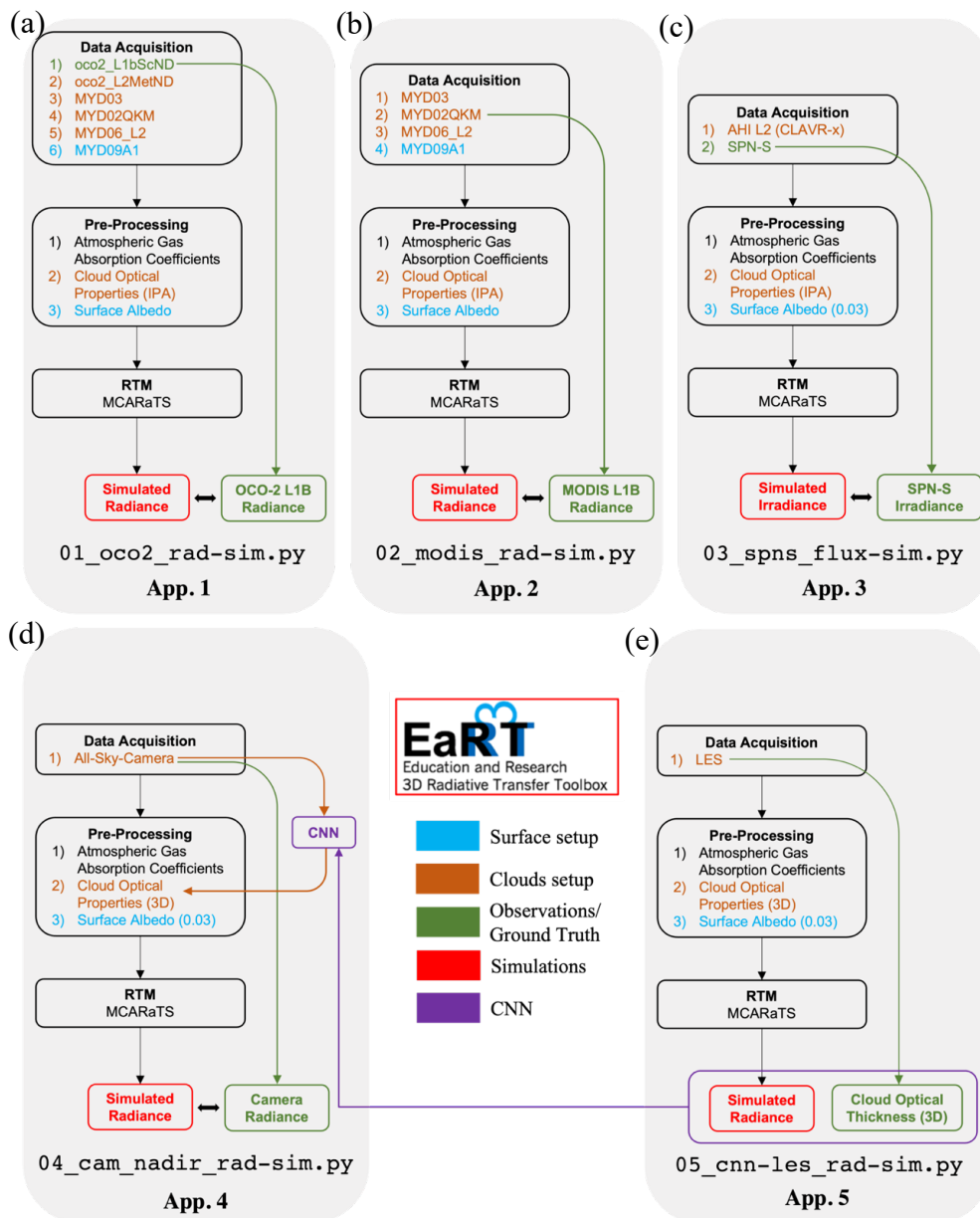
Figure 1. Flow charts of EaR³T applications for (a) OCO-2 radiance simulation at 768.52 nm (data described in section 2.2.1 and 2.2.2, results discussed in section 4.1), (b) MODIS radiance simulation at 650 nm (data described in section 2.2.1, results discussed in section 4.2), (c) SPN-S irradiance simulation at 745 nm (data described in section 2.2.3 and 2.2.4, results discussed in section 5), (d) all-sky camera radiance simulation at 600 nm (data described in section 2.2.5, results discussed in section 6), and (e) radiance simulation at 600 nm based on LES data for CNN training (Appendix B). The data products and their abbreviations are described in section 2.2.

1. App. 1, section 4.1 (`examples/01_oco2_rad-sim.py`): Radiance simulations along the track of OCO-2, based on data products from MODIS and others – to assess consistency (closure) between simulated and measured radiance;

2. App. 2, section 4.2 (`examples/02_modis_rad-sim.py`): MODIS radiance simulations – to assess self-consistency of MODIS level-2 (L2) products with the associated radiance fields (L1B product) under spatially inhomogeneous conditions;

3. App. 3, section 5 (`examples/03_spns_flux-sim.py`): Irradiance simulations along aircraft flight tracks, utilizing the L2 cloud products of the AHI, and comparison with aircraft measurements – to quantify retrieval biases due to 3D cloud structure based with data from an entire aircraft field campaign;

4. App. 4, section 6 (`examples/04_cam_nadir_rad-sim.py`): Mitigation of 3D cloud biases in passive imagery COT retrievals from an airborne camera, application of a convolutional neural network (CNN) and subsequent comparison of CNN-derived radiances with the original measurements – to illustrate how the radiance self-consistency concept assesses the fidelity of cloud retrievals.

5. App. 5, Appendix B (`examples/05_cnn-les_rad-sim.py`): Generation of training data for the CNN (App. 4) based on LES inputs. The training datasets contains 1) the ground truth of COT from the LES data; 2) realistic radiance simulated by EaR³T based on the LES cloud fields.

Figure 1 shows the high-level workflow of the applications. The first four share the general concept of evaluating simulations (the output from the EaR³T, indicated in red at the bottom of each column) with observations (indicated in green at the bottom) from various satellite and aircraft instruments. The workflow of each application consists of three parts – 1) data acquisition, 2) pre-processing, and 3) RTM setup and execution. EaR³T includes functions to ingest data from
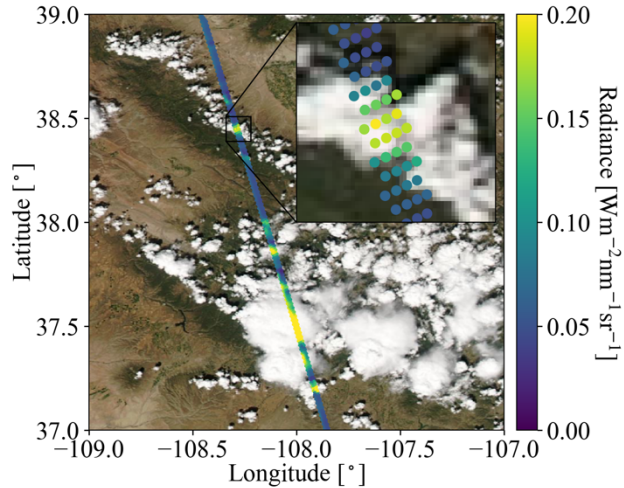
various different sources, e.g., satellite data from publicly available data archives, which can be combined in different ways to accommodate input data depending on the application specifics. For example, in App. 1, EaR^{3}T is used to automatically download and process MODIS and OCO-2 data files based on the user-specified region, date and time. Building on the templates provided in the current code distribution, the functionality can be extended to new spaceborne or airborne instruments. Panel (e) of Figure 1 shows a fifth application that was developed for earlier papers (Gristey et al., 2020a and 2020b; Nataraja et al., 2022; Gristey et al., 2022). In contrast to the first four, which use imagery products as input, the fifth application ingests model output from a Large Eddy Simulation (LES) and produces irradiance data for surface energy budget applications, or synthetic radiance fields for training a CNN. Details and results are described in the respective papers. The remainder of Section 2 introduces the data used in this paper, as well as the input for EaR^{3}T. Subsequently, Section 3 describes the EaR^{3}T procedures.

2.2 Data

The radiance simulations in App. 1 and App. 2 use data from the OCO-2 and MODIS-Aqua instruments, both of which are in a sun-synchronous polar orbit with an early-afternoon equator crossing time within NASA's A-Train satellite constellation. Figure 2 visualizes radiance measurements by OCO-2 in the context of MODIS Aqua imagery over a partially vegetated and partially cloud-covered land, illustrating that MODIS provides imagery and scene context for OCO-2, which in turn observes radiances from a narrow swath. The region is located in southwest Colorado in the United States of America. We selected this case because both the surface and clouds are varied along with diverse surface types. The surface features green forest and brown soil, whereas clouds include small cumulus and large cumulonimbus. In addition, this scene contains relatively homogeneous cloud fields in the north and inhomogeneous cloud fields in the south, which allows us to evaluate the simulations from various aspects of cloud morphology. To simulate the radiances of both instruments we use data products from OCO-2 and MODIS, as well as reanalysis products from NASA's Global Modeling and Assimilation Office (GMAO) sampled at OCO-2 footprints and distributed along with OCO-2 data (section 2.2.2).

Figure 2. OCO-2 measured radiance (units: $Wm^{-2}nm^{-1}sr^{-1}$) at 768.52 nm, overlaid on MODIS Aqua RGB imagery over southwestern Colorado (USA) on 2 September, 2019. The inset shows an enlarged portion along the track, illustrating that OCO-2 radiances co-vary with MODIS-Aqua radiance observations (the circles are used to indicate the geolocation of OCO-2 footprints).

For App. 3 (irradiance simulations and 3D cloud bias quantification), we use geostationary imagery from the Japanese Space Agency's Advanced Himawari Imager to provide cloud information in the area of the flight path of the NASA CAMP^{2}Ex aircraft (Reid et al., 2023). The AHI data are used in conjunction with aircraft measurements of shortwave spectral radiation (section 2.2.4). Subsequently (App. 4: 3D cloud bias mitigation), we demonstrate the concept of radiance closure under partially cloudy conditions with airborne camera imagery (section 2.2.5). The underlying cloud retrieval is based on a convolutional neural network (CNN), which is described in a related paper (Nataraja et al., 2022) in this special issue and relies on EaR^{3}T-generated synthetic radiance data based on Large Eddy Simulations (LES).

2.2.1 Moderate Resolution Imaging Spectroradiometer (MODIS)

The MODIS instruments are multi-use multispectral radiometers onboard NASA's Terra and Aqua satellites, which were launched in 1999 and 2002 respectively. MODIS was conceived as a central element of the Earth Observing System (EOS, King and Platnick, 2018). For App. 1 and App. 2, EaR^{3}T ingests MODIS level 1B radiance products at the quarter kilometer scale (channels 1 and 2, bands centered at 650 and 860 nm), MxD02QKM, where 'x' stands for 'O' in the case of MODIS on Terra, and 'Y' in the case of Aqua data), the geolocation product (MxD03), the level 2 cloud product (MxD06), and the surface BRDF (bidirectional reflectance distribution

265 function) product (MCD43A3). For this paper, we mainly use Aqua data (MYD) from data
266 collection 6.1.

267 For cloud properties in App. 2, we use the MODIS cloud product (MxD06L2, collection
268 6.1). It provides cloud properties such as cloud optical thickness (COT), cloud effective radius
269 (CER), cloud thermodynamic phase, cloud top height (CTH), etc. (Nakajima and King, 1990;
270 Platnick et al., 2003). Since 3D cloud effects such as horizontal photon transport are most
271 significant at small spatial scales (e.g., Song et al., 2016), we use the high-resolution red (650 nm)
272 channel 1 (250 m), and derive COT directly from the reflectance in the Level-1B data
273 (MYD02QKM) instead of using the coarser-scale operational product from MYD06. CER and
274 CTH are sourced from MYD06 and re-gridded to 250 m. The EaR^{3}T strategy for MODIS data is
275 similar, in principle, to the more advanced method by Deneke et al. (2021), which uses a
276 high-resolution wide-band visible channel from geostationary imagery to up-sample narrow-band
277 coarse-resolution channels. However, we simplified cloud detection and COT retrieval (referred
278 to as COT$_{IPA}$) from reflectance data for the purpose of our paper by using a threshold method
279 (Appendix C1) and an IPA reflectance-to-COT mapping (Appendix C2). In future versions of
280 EaR^{3}T this will be upgraded to more sophisticated algorithms. A simple algorithm (Appendix D1)
281 is used to correct for the parallax shift based on the sensor geometries and cloud heights. The cloud
282 top height data is provided by the MODIS L2 cloud product and assuming cloud base is the same.

283 For the surface albedo required by the RTM, we used MCD43A3, which provides BRDF
284 calculated from a combination of Aqua and Terra MODIS and MISR (Multi-Angle Imaging
285 Spectroradiometer) clear-sky observations aggregated over a 16-day period (Strahler et al., 1999).
286 This product contains white sky albedo (WSA, also known as bihemispherical reflectance), which
287 is obtained by integrating the BRDF over all viewing angles (Strahler et al., 1999). The WSA is
288 available on a sinusoidal grid with a spatial resolution of 500 m for MODIS band 2, and includes
289 atmospheric correction for gas and aerosol scattering and absorption. Assuming a Lambertian
290 surface in this first release of EaR^{3}T, we used the WSA (referred to as surface albedo from now
291 on) as surface albedo input to the RTM.

292

2.2.2 Orbiting Carbon Observatory 2 (OCO-2)

294 The OCO-2 satellite was inserted into NASA's A-Train constellation in 2014 and flies
295 about 6 minutes ahead of Aqua. OCO-2 provides the column-averaged carbon dioxide (CO_2)

dry-air mole fraction (XCO_2) through passive spectroscopy based on hyperspectral radiance observations in three narrow wavelength regions, the Oxygen A-Band (~0.76 micron), the weak CO_2 band (~1.60 micron), and the strong CO_2 band (~2.06 micron). As shown in the inset of Figure 2, it takes measurements in eight footprints across a narrow swath. Each of the footprints has a size around 1-2 km, and the spectra for the three bands are provided by separate, co-registered spectrometers (Crisp et al., 2015).

The used OCO-2 data products are 1) Level 1B calibrated and geolocated science radiance spectra (L1bScND), 2) standard Level 2 geolocated XCO_2 retrievals results (L2StdND), 3) meteorological parameters interpolated from GMAO (L2MetND) at OCO-2 footprint location. Since MODIS on Aqua overflies a scene 6 minutes after OCO-2, the clouds move with the wind over this time period. We therefore added a wind correction on top of the parallax-corrected cloud fields obtained from MODIS (section 2.2.1). This was done with the 10 m wind speed data from L2MetND (see Appendix D2). For the same scene as shown in Figure 2, Figure 3 shows (a) COT_{IPA}, (b) CER, and (c) CTH, all corrected for both parallax and wind effects (these corrections are shown in Figure A5 in Appendix D2). The parallax and wind corrections are imperfect as certain assumptions are involved. For example, they rely on the cloud top height from the MODIS cloud product. In addition, they process the whole scene with one single sensor viewing geometry. To minimize artifacts introduced by the assumptions, one can apply the simulation to a smaller region.
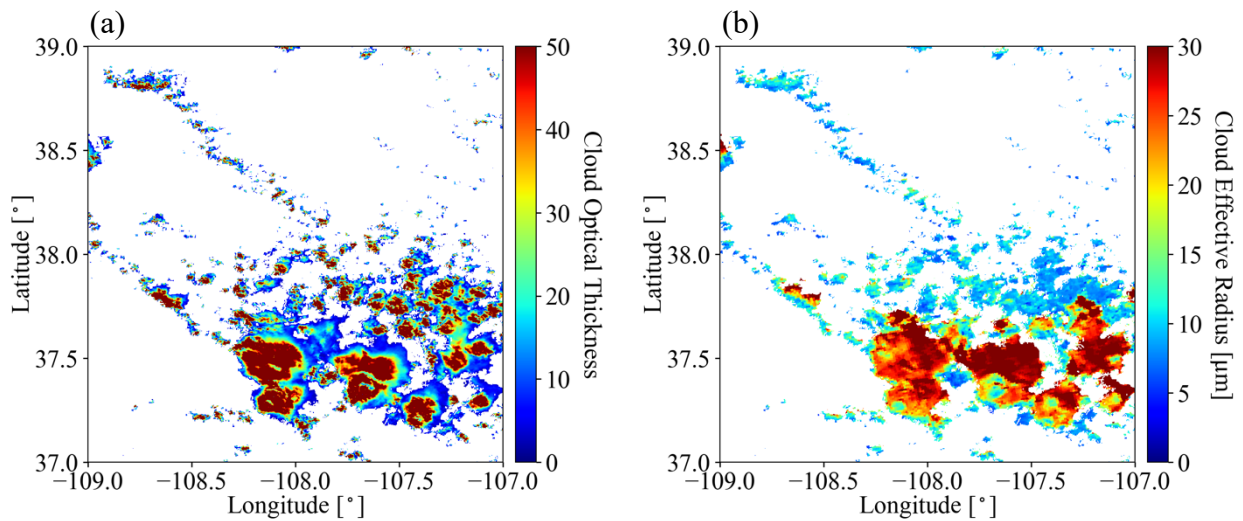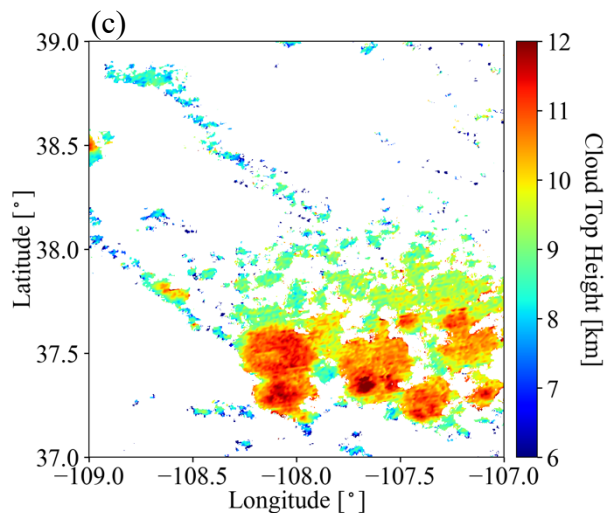
Figure 3. **(a)** Cloud optical thickness derived from MODIS L1B radiance at 650 nm by the IPA reflectance-to-COT mapping (Appendix C2), **(b)** cloud effective radius (units: μm), and **(c)** cloud top height (units: km) collocated from the MODIS L2 cloud product. The locations of the cloudy pixels were shifted to account for parallax and wind effects. The parallax correction ranged from near 0 for low clouds and 1 km for high clouds (10 km CTH). The wind correction was around 0.8 km, given the median wind speed of 2 m/s to the east.

The OCO-2 data (L2StdND) themselves only provide sparse surface BRDF (referred to as surface albedo from now on) for the footprints that are clear, while EaR³T requires surface albedo for the whole domain. Therefore, we used MCD43A3 as a starting point. However, since MODIS does not have a channel in the Oxygen A-Band, MODIS band 2 (860 nm) was used as a proxy for the 760 nm OCO-2 channel as follows: we collocated the OCO-2 retrieved 760 nm surface albedo α_{OCO} within the corresponding 860 nm MODIS MCD43A3 data α_{MOD} as shown in Figure 4a (same domain as Figures 2 and 3) and calculated a scaling factor assuming a linear relationship between α_{OCO} and α_{MOD} ($\alpha_{OCO} = c \cdot \alpha_{MOD}$). Figure 4b shows α_{OCO} versus α_{MOD} for all cloud-free OCO-2 footprints. The red line shows a linear regression (derived scale factor *c=0.867*). Optionally, the OCO-2-scaled MODIS-derived surface albedo fields can be replaced by the OCO-2 surface albedo products for pixels where they are available. The replacement is done for App. 1. The scaled and replaced surface albedo is then treated as input to the RTM assuming a Lambertian surface.
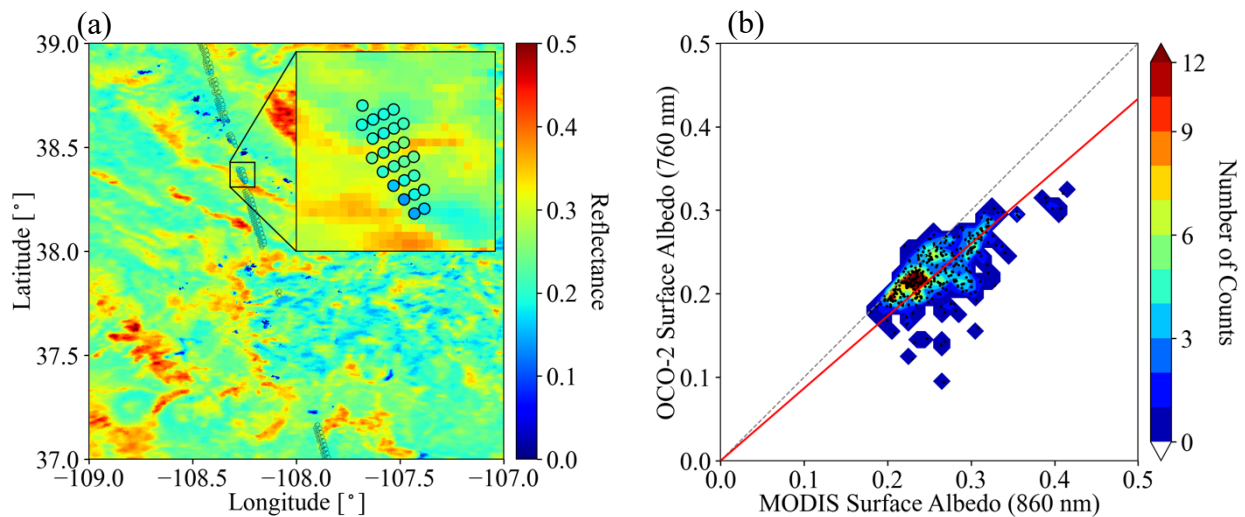
Figure 4. **(a)** Surface albedo from the OCO-2 L2 product in the Oxygen A-band (near 760 nm), overlaid on the surface albedo from the MODIS MCD43A3 product at 860 nm. **(b)** OCO-2 surface albedo at 760 nm versus MODIS surface albedo at 860 nm, along with linear regression ($\alpha_{OCO} = c \cdot \alpha_{MOD}$) as indicated by the red line (slope $c=0.867$).

2.2.3 Advanced Himawari Imager (AHI)

The Advanced Himawari Imager (AHI, used for App. 3) is a payload on Himawari-8, a geostationary satellite operated by the Meteorological Satellite Center (MSC) of the Japanese Meteorological Agency. The AHI provides 16 channels of spectral radiance measurements from the shortwave (0.47μm) to the infrared (13.3μm). During CAMP^{2}Ex, the NASA in-field operational team closely collaborated with the team from MSC to provide AHI satellite imagery at the highest resolution over the Philippine Sea. From the AHI imagery, the cloud product generation system - Clouds from AVHRR Extended System (CLAVR-x), was used to generate cloud products from the AHI imagery (Heidinger et al., 2014). The cloud products from CLAVR-x include cloud optical thickness, cloud effective radius, and cloud top height at 2 (at nadir) to 5 km spatial resolution. Since AHI provides continuous regional scans every 10 minutes the AHI cloud product has a temporal resolution of 10 minutes.

2.2.4 Spectral Sunshine Pyranometer (SPN-S)

The SPN-S is a prototype spectral version of the commercially available global-diffuse SPN1 pyranometer (Wood et al., 2017; Norgren et al., 2022). The radiometer uses a 7-detector design in combination with a fixed shadow mask that enables the simultaneous measurement of both diffuse and global irradiances, from which the direct component of the global irradiance is

14

363　　calculated via subtraction. The detector measures spectral irradiance from 350 to 1000 nm, and the

364　　spectrum is sampled at 1 nm resolution with 1 Hz timing.

365　　　　　During the CAMP^{2}Ex mission, the SPN-S was mounted to the top of the NASA P-3 aircraft

366　　where it sampled downwelling solar irradiance. To ensure accurate measurements, pre- and

367　　post-mission laboratory-based calibrations were completed using tungsten "FEL" lamps that are

368　　traceable to a National Institute of Standards and Technology standard. Additionally, the direct

369　　and global irradiances were corrected for deviations of the SPN-S sensor plane from horizontal

370　　that are the result of changes in the aircraft's pitch or roll. This attitude correction applied to the

371　　irradiance data is a modified version of the method outlined in Long et al. (2010). However,

372　　whereas Long et al. (2010) employ a "box" flight pattern to characterize the sensor offset angles,

373　　in this study an aggregation of flight data containing aircraft heading changes under clear-sky

374　　conditions are used as a substitute. The estimated uncertainty of the SPN-S system is 6 to 8%, with

375　　4 to 6% uncertainty stemming from the radiometric lamp calibration process, and up to another 2%

376　　resulting from insufficient knowledge of the sensor cosine response. The stability of the system

377　　under operating conditions is 0.5%. A thorough description of the SPN-S and its calibration and

378　　correction procedures is provided in Norgren et al. (2022). In this paper (App. 3) only the global

379　　downwelling irradiance sampled by the 745 nm channel is used.

380

381　　**2.2.5 Airborne All-Sky Camera (ASC)**

382　　　　　The All-Sky Camera (used for App. 4) is a commercially available camera (ALCOR

383　　ALPHEA 6.0CW[5]) with fish-eye optics for hemispheric imaging. It has a Charge-Coupled Device

384　　(CCD) detector that measures radiances in red, green, and blue channels. Radiometric and

385　　geometric calibrations were performed at the Laboratory of Atmospheric and Space Physics at the

386　　University of Colorado Boulder. The three-color channels are centered at 493, 555, and 626 nm

387　　for blue, green, and red, respectively, with bandwidths of 50 – 100 nm. Only radiance data from

388　　the red channel are used in this paper. The spatial resolution of the ASC depends on the altitude of

389　　the aircraft and the viewing zenith angle. Across the hemispheric field of view of the camera, the

390　　resolution of the field angle is approximately constant, at about 0.09º. At a flight level of 5 km,

---

[5]https://www.alcor-system.com/common/allSky/docs/ALPHEA_Camera%20ALL%20SKY%20CAMERA_Doc.pdf
last accessed on April 24, 2022.

391   this translates to a spatial resolution of 8 m at nadir. However, due to accuracy limitations of the
392   geometric calibration and the navigational data from Inertial Navigation System (INS), the nadir
393   geolocation accuracy could only be verified to within ±50 m. During the CAMP²Ex flights, the
394   camera exposure time was set manually to minimize saturation of the detector. The standard image
395   frame rate is 1 Hz. The precision of the camera radiances is on the order of 1%, and the radiometric
396   accuracy is 6 – 7%.

397

398   **3. EaR³T Procedures**

399   In the previous section, we described the input data for the EaR³T applications. In this
400   section, we will focus on providing the complete workflow (shown in Figure 1) for the five
401   applications.

402   After the required data files have been automatically downloaded in the data acquisition
403   step as described in previous section, EaR³T pre-processes them and generates the optical
404   properties of atmospheric gases, clouds, aerosols, and the surface. In Figure 1, the mapping from
405   input data to these properties is color-coded component-wise (brown for associated cloud property
406   processing if available, blue for associated surface property processing if available, green for
407   associated ground truth property). The EaR³T code base used in this paper (v0.1.1; Chen and
408   Schmidt, 2022) only includes MCARaTS as the 3D RT solver, but others are planned for the future.
409   MCARaTS is a radiative transfer solver that uses a Monte Carlo photon-tracing method (Iwabuchi,
410   2006). It outputs radiation (radiance or irradiance) based on the inputs of radiative properties of
411   surface and atmospheric constituents (e.g., gases, aerosols, clouds) such as single scattering albedo,
412   scattering phase function or asymmetry parameter, along with solar and sensor viewing geometries.
413   The setup of these input properties is implemented in EaR³T's pre-processing steps, which
414   translates atmospheric properties into solver-specific input with minimum user intervention. To
415   achieve this, EaR³T is modular so that it can be extended as new solvers are added. Although the
416   five specific applications in this paper do not include aerosol layers, the setup of aerosol fields is
417   fully supported and has been used in other applications (e.g., Gristey et al., 2022). After pre-
418   processing, the optical properties are fed into the RT solver. Finally, the user obtains radiation
419   output from EaR³T, either radiance or irradiance. The output is saved in HDF5 format and can be
420   easily distributed and accessed by various programming languages. The data variables contained
421   in the HDF5 output are provided in Table A2 in Appendix A1.

422   The processes of data acquisition, pre-processing, and RTM setup and execution (shown
423 in Figure 1) are automated such that the 3D/1D-RT calculations can be performed for any region
424 at any date and time using satellite or aircraft data or other data resources such as LES. A detailed
425 code walk-through of App. 1 and 2 is provided in Appendix A2. Since EaR³T is developed as an
426 educational and research 3D-RT tool collection by students, it is a living code base, intended to be
427 updated over time. The master code modules for the five applications as listed in Figure 1 are
428 included in the EaR³T package under the `examples` directory. In the current release (v0.1.1),
429 only a limited documentation for the installation and usage, including example code for EaR³T, is
430 provided. More effort will be dedicated for documentation in the near-future.

431   In the following sections, we discuss results obtained from EaR³T, starting with those from
432 `examples/01_oco2_rad-sim.py` and `examples/02_modis_rad-sim.py` (section
433 4), `examples/03_spns_flux-sim.py` (section 5), and concluding with
434 `examples/04_cam_nadir_rad-sim.py` (section 6). The usage of the EaR³T package
435 including the technical input and output parameters and code walk-through is provided in
436 Appendix A.

437

4. EaR³T as a 3D Satellite Radiance Simulator

439   This section demonstrates the automated 3D radiance simulation for satellite instruments
440 by EaR³T for OCO-2 and MODIS measured radiance based on publicly available MODIS retrieval
441 products. The OCO-2 application is an example of radiance consistency between two distinct
442 satellite instruments where the measurements of one (here, OCO-2) are compared with the
443 simulations based on data products from the other (here, MODIS). The MODIS application, on
444 the other hand, is an example of radiance self-consistency. We will show how inconsistencies can
445 be used for detecting cloud and surface property retrieval biases.

4.1 OCO-2 (App. 1)

447   The OCO-2 radiance measurements at 768.52 nm for our sample scene in the context of
448 MODIS imagery were shown in Figure 2. For that track segment, Figure 5a shows the simulated
449 radiance along with the measurements as a function of latitude. The radiance was averaged over
450 every 0.01° latitude window from 37° N to 39° N (the standard deviation within the bin indicated
451 by the shaded color). In clear-sky regions (e.g., around 38.2º N), the 3D simulations (red) are
452 systematically higher than the measurements (black), even though the footprint-level OCO-2

surface albedo retrieval was used to replace and scale the MCD43 surface albedo field as described in section 2.2.2 (Figure 4). This is probably because, unlike the MCD43 algorithm which relies on multiple overpasses and multiple-days for cloud-clearing, the OCO-2 retrieval is done for any clear footprint. Clouds in the vicinity lead to enhanced diffuse illumination that is erroneously attributed to the surface albedo itself. The EaR^{3}T IPA calculations of the clear-sky pixels (blue) essentially reverse the 3D effect and therefore match the observations better. The 3D calculations enhance the reflectance through the very same 3D cloud effects that led to the enhanced surface illumination in the first place. It is possible to correct this effect by down-scaling the surface albedo according to the ratio between clear-sky 3D and IPA calculations, but this process is currently not automated.
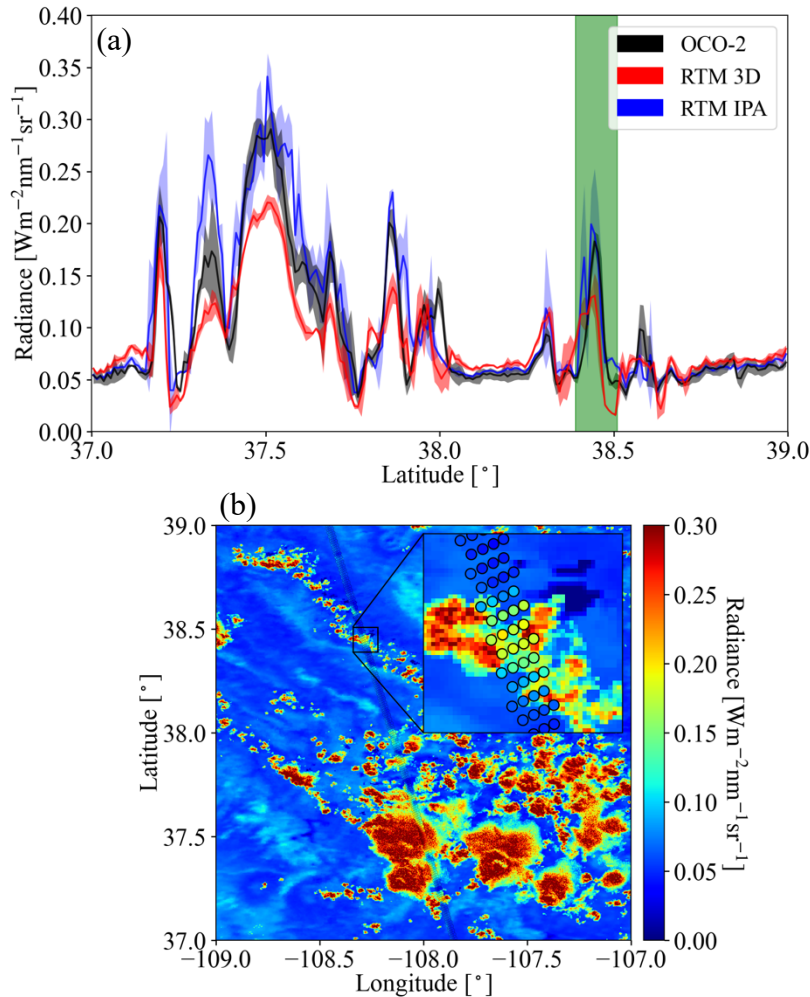
Figure 5. **(a)** Latitudinally averaged (0.01° spacing) radiance calculations from EaR^{3}T (red: 3D, blue: IPA) and OCO-2 measured radiance at 768.52 nm (black) The green shaded area indicates the inset shown in (b). **(b)** The

18

467   same as Figure 2 except OCO-2 measured radiance overlaid on IPA radiance simulations at 768.52 nm. The

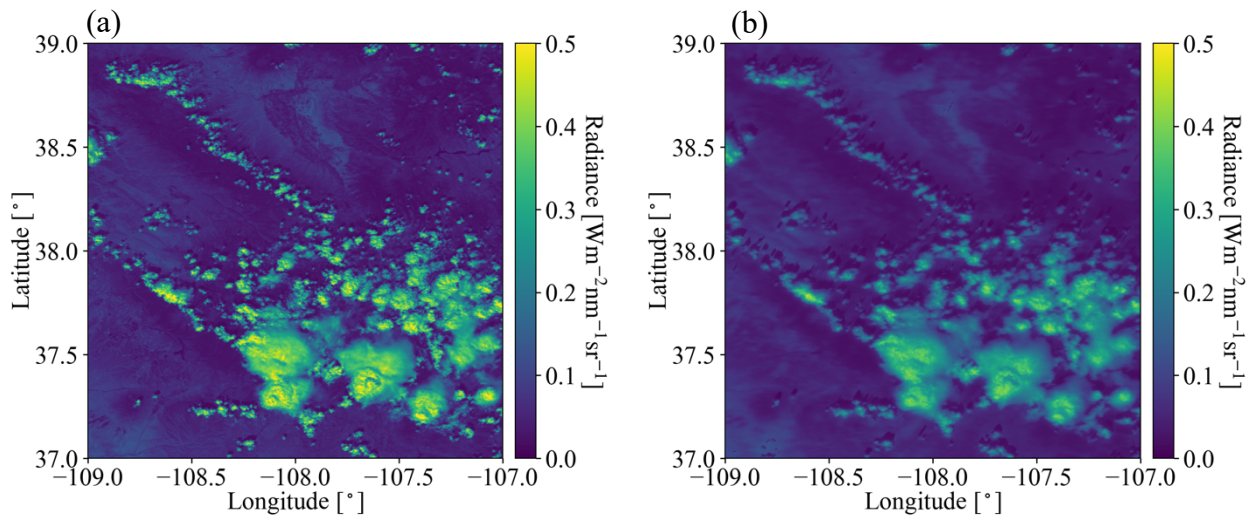468   solar zenith angle (SZA) for the radiance simulation case is 34.3°.

469

470   In the cloudy locations (radiance value greater than ~0.05), the IPA calculations match the

471   OCO-2 observations on a footprint-by-footprint level (see Figure 5b), demonstrating that wind and

472   parallax corrections were performed successfully. Of course, there is not always a perfect

473   agreement because of morphological changes in the cloud field over the course of six minutes. It

474   is, however, apparent that the 3D calculations agree to a much lesser extent with the observations

475   than the IPA calculations. Just like the mismatch for the clear-sky pixels indicates a bias in the

476   input surface albedo, the bias here means that the input cloud properties (most importantly COT)

477   are inaccurate. For most of the reflectance peaks, the 3D simulations are too low, which means

478   that the input COT is biased low. This is due to 3D cloud effects on the MODIS-based cloud

479   retrieval. Since they are done with IPA, any net horizontal photon transport is not considered,

480   which leads to an apparent surface brightening as noted above, at the expense of the cloud

481   brightness. As a result, the COT from darker clouds is significantly underestimated. This

482   commonly known problem (Barker and Liu, 1995), with several aspects discussed in the

483   subsequent EaR[3]T applications, can be identified by radiance consistency checks such as the one

484   shown in Figure 5, and mitigated by novel types of cloud retrievals that do take horizontal photon

485   transport into account (section 6).

486

4.2 MODIS (App. 2)

488   To go beyond the OCO-2 track and understand the bias between simulated and observed

489   radiances from a domain perspective, we now consider the radiance simulations for the MODIS

490   650 nm channel. The setup is exactly the same as for the OCO-2 simulations, except that 1) the

491   viewing zenith angle is set to the average viewing zenith angle of MODIS within the shown domain

492   (instead of OCO-2), and 2) the surface albedo (or WSA) from MCD43 is used directly, this time

493   from the 650 nm channel without rescaling. Figure 6a shows the MODIS measured radiance field,

494   while Figure 6b shows the EaR[3]T 3D simulations. Visually, the clouds from the EaR[3]T simulation

495   are generally darker than the observed clouds, which is in line with our aforementioned explanation

496   of net horizontal photon transport. They are also blurrier because radiative smoothing (Marshak et

497   al., 1995) propagates into the retrieved COT fields, which are subsequently used as input to EaR[3]T.

498   The IPA RT calculations agree with the observations for clouds (see Figure A4a in Appendix C2),

499   which is expected as the IPA calculations and retrievals go through the same RT process, and the

500   darkening and smoothing effects (referred to as 3D effects) are due to horizontal photon transport.

501   To look at the 3D effects more quantitatively, Figure 7 shows a heatmap plot of simulated radiance

502   versus observed radiance. It shows that the radiance for cloud-covered pixels (labeled "cloudy")

503   from EaR^{3}T are mostly low-biased while good agreement between simulations and observations

504   was achieved for clear-sky radiance (labeled "clear-sky"). The good agreement over clear-sky

505   regions is expected. As mentioned above, we use MCD43 as surface albedo input, which in

506   contrast to the OCO-2 surface albedo product is appropriately cloud-screened and therefore does

507   not have a reflectance high bias. There is, of course, a reflectance enhancement in the vicinity of

508   clouds, but that is captured by the EaR^{3}T calculations. The fact that the calculations agree with the

509   observations even for clear-sky pixels in the vicinity of clouds, shows that the concept of radiance

510   consistency works to ensure correct satellite retrievals even in the presence of clouds. It also

511   corroborates our observation from section 4.1 that COT_{IPA} is low biased. Since the MODIS

512   reflectance is *not* self-consistent with respect to 3D RT calculations using COT_{IPA} as shown for

513   the *cloudy* pixels in Figure 7, we can identify a bias in the cloud properties even without knowing

514   the ground truth of COT. On the other hand, successful closure in radiance (self-consistency)

515   would provide an indication that the input fields including COT are accurate, although it is

516   certainly a weaker metric than direct verification of the retrievals through aircraft-satellite retrieval

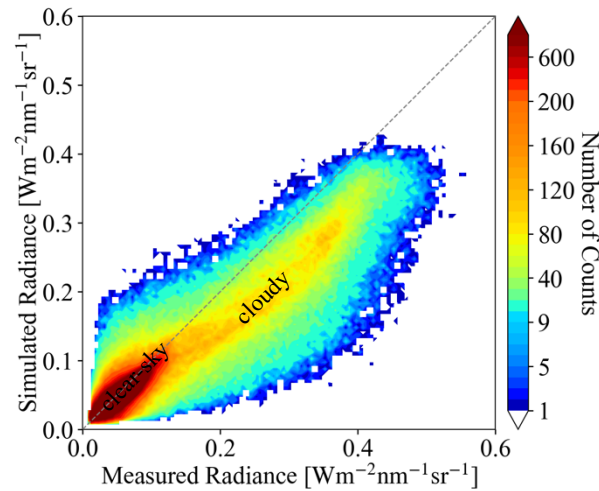517   validation using observations from in-situ instruments.

518

519

520 **Figure 6**. **(a)** MODIS measured radiance in channel 1 (650 nm). **(b)** Simulated 3D radiance at 650 nm from EaR³T.
521   The solar zenith angle for the radiance simulation case is 34.94°.

522
523

524
525 **Figure 7**. Heatmap plot of EaR³T simulated 3D radiance vs. MODIS measured radiance at 650 nm.

526

527   Summarizing the two satellite radiance simulator applications, one can say that EaR³T
528 enables a radiance consistency check for inhomogeneous cloud scenes. We demonstrated that a
529 lack of simulation-observation consistency (MODIS versus OCO-2) and self-consistency (MODIS
530 versus MODIS) can be traced back to biased surface albedo or cloud fields in the simulator input.
531 This can become a diagnostic tool for the quality of retrieval products from future or current
532 missions, even when the ground truth is not known. Although not shown, the errors in the
533 simulated radiance associated with the fixed-SZA assumption (domain average) are negligible.
534 However, the vertical extent of the clouds affects the simulated radiance – the larger the vertical
535 extent, the larger the 3D effects (more horizontal photon transport). Since we make the assumption
536 of 1) a cloud geometric thickness of 1 km for clouds with CTH less than 4 km, and 2) cloud base
537 height of 3 km for clouds with CTH greater than 4km, the simulated radiance at the satellite sensor
538 level is valid for that proxy cloud only. For clouds that are geometrically thicker than the assumed
539 cloud geometrical thickness, the simulated radiance would be even lower due to enhanced
540 horizontal photon transport. Either way, the comparison with the actual radiance measurements
541 will reveal a lack of closure. Additionally, although the clouds introduce the lion's share of the 3D
542 bias that is identified by the radiance consistency check, additional discrepancies can be introduced

21

543   in different ways. For example, the topography (mountainous region in Colorado) is not considered

544   by MCARaTS (it is considered by MYSTIC, but this solver has not been implemented yet).

545   For the reference of simulation running time: The MODIS simulation (domain size of

546   [Nx=846, Ny=846]) took about 15 minutes on a Linux workstation with 8 CPUs for three 3D RT

547   runs with 10^8 photons. With a slightly modified setup and parallelization, the automation can be

548   easily applied for entire satellite orbits, although more research is required to optimize the

549   computation speed depending on the desired output accuracy.

550

5. EaR³T as 3D Aircraft Irradiance Simulator (App. 3)

552   In contrast to the previous applications that focused on satellite remote sensing, we will

553   now be applying EaR³T to quantify 3D cloud retrieval biases through direct, systematic validation

554   of imagery-derived *irradiances* against aircraft measurements, instead of using the indirect path

555   of radiance consistency in section 4. Previous studies (e.g., Schmidt et al., 2007; Kindel et al.,

556   2010) conducted radiative closure between remote sensing derived and measured irradiance using

557   isolated flight legs as case studies. Here, with the efficiency afforded by the automated nature of

558   EaR³T, we are able to conduct radiative closure of irradiance through a statistical approach that

559   employs campaign-scale amounts of measurement data. Specifically, we used EaR³T to perform

560   large-scale downwelling irradiance simulations at 745 nm based on geostationary cloud retrievals

561   from AHI for the CAMP²Ex campaign, and directly compare these simulations to the SPN-S

562   measured irradiances onboard the P-3 aircraft. This is done for all below-cloud legs from the entire

563   campaign with the aim to assess the degree to which satellite-derived near-surface irradiances

564   reproduce the true conditions below clouds.

565   The irradiance simulation process is similar to the previously described radiance simulation

566   in section 4, with only a few modifications. First, we used cloud optical properties from the AHI

567   cloud product (COT, CER and CTH) as direct inputs into EaR³T. Secondly, we used a constant

568   ocean surface albedo value of 0.03. Such simplification in surface albedo is made under the

569   assumption that 1) the ocean surface is calm with no whitecaps, and that 2) the Lambertian BRDF

570   is sufficient (instead of directionally dependent BRDF) to represent surface albedo for the

571   irradiance calculation. Since the ocean surface albedo can greatly differ from 0.03 when the Sun

572   is extremely low (Li et al., 2006), we excluded data under low-Sun conditions where the SZA is

573   greater than 45°. Lastly, since EaR³T can only perform 3D simulations for a domain at a single

574   specified solar geometry, we divided each CAMP[2]Ex research flight into small flight track

575   segments where each segment contains 6 minutes of flight time. The size and shape of the flight

576   track segments can vary significantly due to the aircraft maneuvers, aircraft direction, aircraft

577   speed, etc. For each flight track segment, EaR^{3}T performs irradiance simulations for a domain that

578   extends half a degree at an averaged solar zenith angle. In contrast to the radiance simulation output,

579   which is two-dimensional at a specified altitude and sensor geometry, the irradiance simulation

580   output is three dimensional. In addition to x (longitude) and y (latitude) vectors, it has a vertical

581   dimension along z (altitude). From the simulated three-dimensional irradiance field, the irradiance

582   for the flight track segment is linearly interpolated to the x-y-z location (longitude, latitude, and

583   altitude) of the aircraft. EaR^{3}T automatically sub-divides the flight track into tiles encompassing

584   track segments, and extracts the necessary information from the aircraft navigational data. Based

585   on the aircraft time and position, EaR^{3}T downloads the AHI cloud product that is closest in time

586   and space to the domain containing the flight track segment.

587   Figure 8 shows the simulated irradiance for a sample flight track below clouds on 20

588   September, 2019. Figure 8a shows the flight track overlaid on AHI imagery. Figure 8b shows 3D

589   (in red) and IPA (in blue) downwelling irradiance simulations for the highlighted flight track in

590   Figure 8a, as well as measurements by the SPN-S (in black). Since the 3D and IPA simulations

591   are performed separately at discrete solar and sensor geometries for each flight track segment based

592   on potentially changing cloud fields from one geostationary satellite image to the next,

593   discontinuities in the calculations (indicated by gray dashed lines) are expected. The diffuse

594   irradiance (downwelling and upwelling) can also be simulated and compared with radiometer

595   measurements (not shown here). Since the irradiance was simulated/measured below clouds, high

596   values of downwelling irradiance indicate thin-cloud or cloud-free regions while low values of

597   downwelling irradiance indicate thick-cloud regions. The simulations successfully captured this

598   general behavior – clouds thickened from west to east until around 121.25° E, and thinned

599   eastwards. However, the fine-scale variabilities in irradiance were not captured by the simulations

600   due to the coarse resolution of COT in the AHI cloud product (3-5 km). Additionally, the

601   simulations also missed the clear-sky regions in the very east and west of the flight track as

602   indicated by high downwelling irradiance values measured by SPN-S. This is probably also due to

603   the coarse resolution of the AHI COT product where small cloud gaps are not represented. Large

604   discrepancies between simulations and observations occur in the mid-section of the flight track

605   where clouds are present (e.g., longitude range from 121.15° to 121.3°). Although the 3D

606   calculations differ somewhat from the IPA results, they are both biased high, likely because the

607   input COT (the IPA-retrieved AHI product) is biased low. This bias is caused by the same

608   mechanism that was discussed earlier in the MODIS examples (section 4.2). This begs the question

609   whether this is true for the entire field mission. To answer the question, we performed a *systematic*

610   comparison of the cloud transmittance for *all* available below-cloud flight tracks from CAMP[2]Ex,

611   using EaR[3]T's automated processing pipeline. The output of this pipeline is visualized in time-

612   synchronized flight videos (Chen et al., 2022), which show the simulations and observations along

613   all flight legs point by point. These videos give a glimpse of the general cloud environment during

614   the field campaign from the geostationary satellite perspective.

615

616
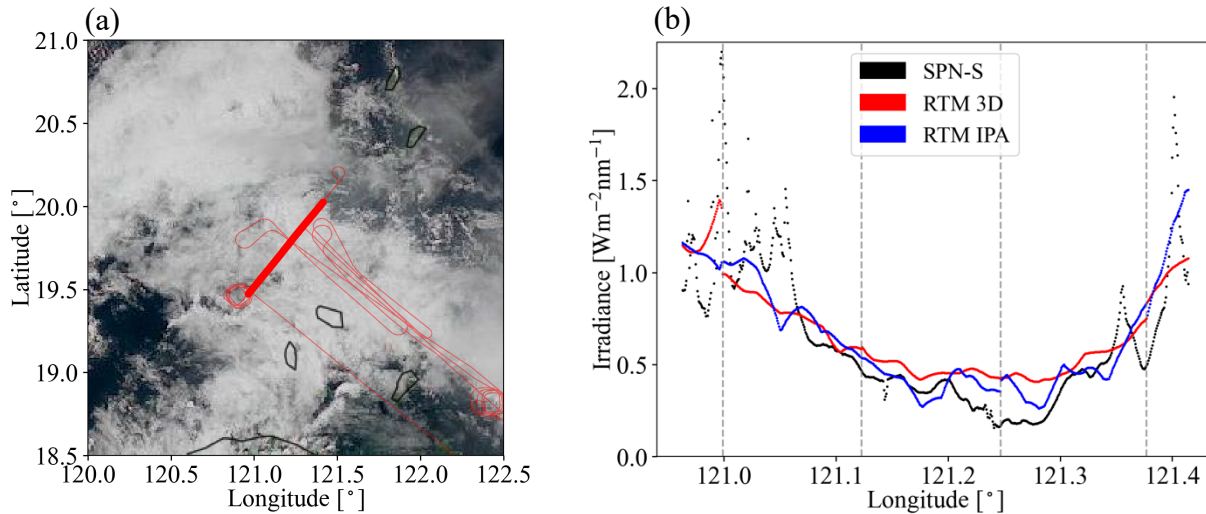
618 **Figure 8**. **(a)** Flight track overlay HIMAWARI AHI RGB imagery over the Philippine Sea on 20 September, 2019.
619   The thin line shows the entire flight track within the domain. The thick line highlights the specific leg
620   analyzed in (b). **(b)** Measured downwelling irradiance from SPN-S at 745 nm and calculated 3D and IPA
621   irradiance from EaR[3]T for the highlighted flight track in (a).

622

623   For this comparison, we use transmittance instead of irradiance. The transmittance is

624   calculated by dividing the downwelling irradiance below clouds ($F_\downarrow^{bottom}$) by the downwelling

625   irradiance at the top of the atmosphere extracted from the Kurucz solar spectra ($F_\downarrow^{TOA}$; Kurucz,

626   1992) at incident solar zenith angle (SZA), where

24

$$627 \quad Transmittance = \frac{F_\downarrow^{bottom}}{F_\downarrow^{TOA} \cdot \cos(SZA)}$$

628   Thus the transmittance has less diurnal dependence than the irradiance. Figure 9 shows the

629   histograms of the simulated and measured cloud transmittance from all below-cloud legs. The

630   average values are indicated by dashed lines. Although the averaged values of IPA and 3D

631   transmittance are close, their distributions are different. Only the 3D calculations and the measured

632   transmittance reach values beyond 1. This occurs in clear-sky regions in the vicinity of clouds that

633   receive photons scattered by the clouds as previously discussed for the OCO-2 application.

634
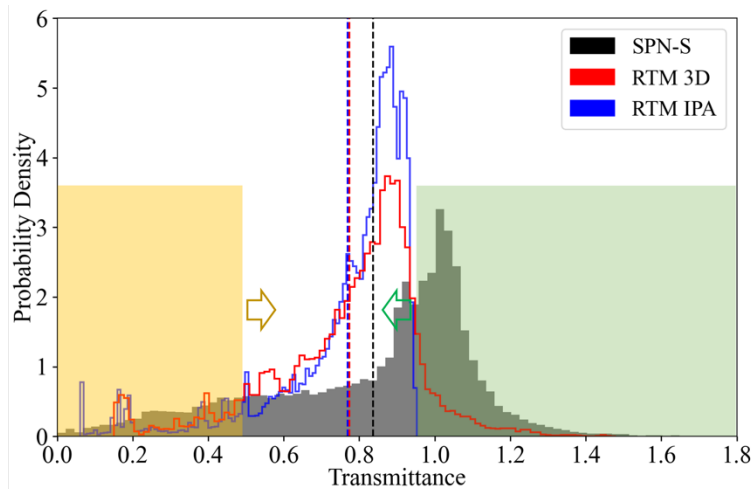
635

636   **Figure 9**. Histogram of measured transmittance from SPN-S at 745 nm (dark gray filled) and calculated 3D (red solid

637   line) and IPA (blue solid line) transmittance from EaR³T for all the below-cloud flight tracks during

638   CAMP²Ex in 2019. The mean values are indicated by dashed lines. The yellow (green) shaded area

639   represents the relatively low (high) transmittance region where the probability density of the observed

640   transmittance (dark gray filled) is greater than the calculations.

641

642   Both the distribution and the mean value of the simulations are different from the

643   observations – the simulation histograms peak at around 0.9 while the observation histogram peaks

644   at around 1. The histograms indicate that the RT simulations miss most of the clear-sky conditions

645   because of the coarse resolution of the AHI cloud product. If clouds underfill a pixel, AHI

646   interprets the pixel as cloudy in most cases. This leads to an underestimation of clear-sky regions

647   since cumulus and high cirrus were ubiquitous during CAMP²Ex. The area on the left (highlighted

648   in yellow) has low cloud transmittance associated with thick clouds. In this range, the histograms

649   of the calculations are generally below the observations, and the PDF of the calculations is offset

650   to the right (indicated by the yellow arrow). This means that the transmittance is overestimated by

651   both IPA and 3D RT, and thus that the COT of thick clouds is underestimated, consistent with

652   what we found before (Figure 8b). The high-biased transmittance below-cloud is also consistent

653   with the findings of low-biased reflectance (App. 1 and 2), both indicating COT of the optically

654   thick clouds are low-biased. The high-transmittance end (highlighted in green) is associated with

655   clear-sky and thin clouds. Here, the peak of the PDF is shifted to the left (green arrow), and the

656   calculations are biased low. This is caused by a combination of 1) the overestimation in COT of

657   thin clouds due a 3D bias in the AHI IPA retrieval, 2) the aforementioned resolution effect that

658   underestimates the occurrence of clear-sky regions (or overestimation in cloud fraction), and 3)

659   net horizontal photon transport from clouds into clear-sky pixels. Overall, the calculations

660   underestimate the true transmittance by 10%. This might seem to contradict Figure 7, where the

661   calculated reflected radiance was biased low due to the *underestimation* of COT in the heritage

662   retrievals, which would correspond to an *overestimation* of the radiation transmitted by clouds.

663   This effect is indeed apparent in the yellow-shaded area of Figure 9 (high COTs), but the means

664   (dashed lines) show exactly the opposite. To understand that, one has to consider that the histogram

665   depicts all-sky conditions, which include both cloudy and clear pixels. In this case, the direction

666   of the overall (all-sky) bias follows the direction of the thin-cloud/clear bias, rather than the

667   direction of the thick cloud bias. For different study regions of the globe with different cloud

668   fractions, cloud size distributions, and possibly different imager resolutions, the direction and

669   magnitude of the bias might be very different.

670   Summarizing, this application demonstrates that the EaR^{3}T's automation feature allows

671   systematic simulation-to-observation comparisons. If aircraft observations are available, then

672   closure between satellite-derived irradiance and suborbital measurements is a more powerful

673   verification of satellite cloud retrieval products than the radiance consistency from the earlier

674   stand-alone satellite applications. Even more powerful is the new approach to process the data

675   from an entire field mission for assessing the quality of cloud products in a region of interest (in

676   this case, the CAMP^{2}Ex area of operation).

677

678   **6. EaR^{3}T for Mitigating 3D Cloud Retrieval Biases (App. 4)**

679   In this section, we will use high-resolution imagery from a radiometrically calibrated

680   all-sky camera flown during the CAMP^{2}Ex to isolate the 3D bias (sometimes referred to as IPA

681   bias) and explore its mitigation with a newly developed CNN cloud retrieval framework (Nataraja

682   et al., 2022). The CNN, unlike IPA, takes pixel-to-pixel net horizontal photon transport into

683   account. It exploits the spatial context of pixels in cloud radiance imagery, and extracts a higher-

684   dimensional, multi-scale representation of the radiance to retrieve COT fields as the output. It does

685   so by learning on "training data", which in this case was input radiance and COT pairs synthetically

686   generated by EaR^{3}T using LES data from the Sulu Sea. The best CNN model, trained on different

687   coarsened resolutions of the data pairs, is included within the EaR^{3}T repository. For App. 4, this

688   CNN is applied to real imagery data for the first time, which in our case are near-nadir observations

689   by the all-sky camera (section 2.2.5) that flew in CAMP^{2}Ex.

690   The CNN model was trained at a single (fixed) sun-sensor geometry (solar zenith angle,

691   SZA=29.2°; solar azimuth angle, SAA=323.8°, viewing zenith angle, VZA=0º), at a spatial

692   resolution of 100 m. We therefore chose a camera scene with a matching SZA (28.9°), and rotated

693   the radiance imagery to match SAA=323.8°, and subsequently gridded the 8-12 m native

694   resolution camera data to 100 m. Figure 10a shows the RGB imagery captured by the all-sky

695   camera over the Philippine Sea at 02:10:06 UTC on 5 October 2019. The Sun is located at the

696   southeast (as indicated by the yellow arrow) and can be easily identified from the sun glint. Note

697   that this image has not yet been geolocated; it is depicted as acquired in the aircraft reference frame.

698   Figure 10b shows the rotated scene of the red channel radiance for the region encircled in yellow

699   in Figure 10a. The sun (as indicated by the yellow arrow) is now at SAA=323.8°. The selected

700   study region is indicated by the red rectangle in Figure 10b (6.4x6.4 km^2), where the raw radiance

701   of the camera is gridded at 100 m resolution to match the spatial resolution of the training dataset

702   of the CNN.

703

704

(a)

(b)
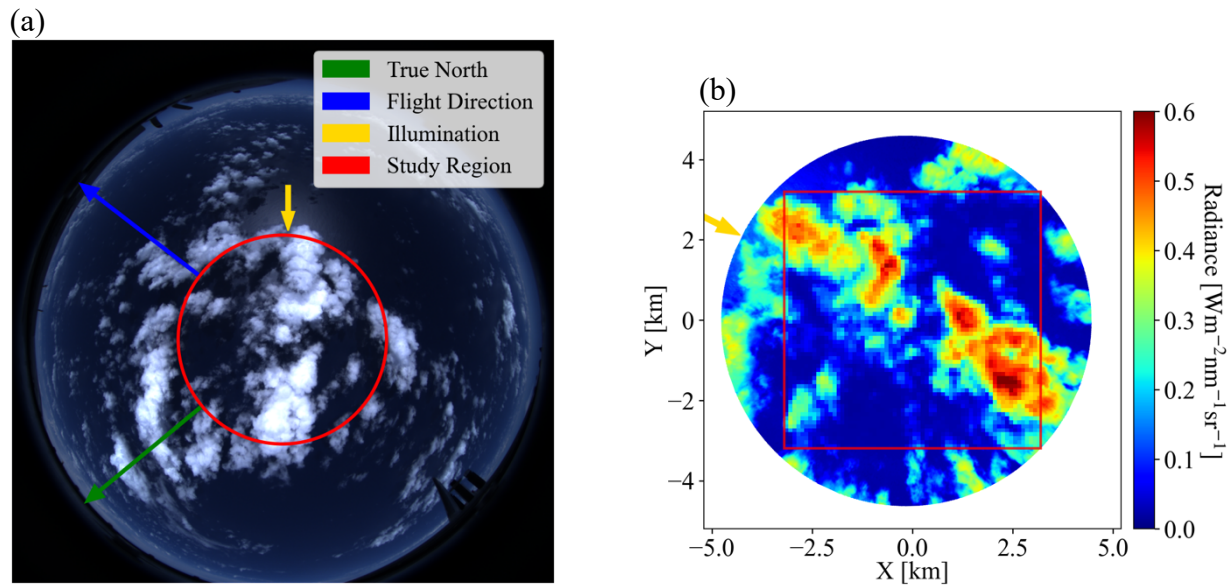
Figure 10. **(a)** RGB imagery of nadir-viewing all-sky camera deployed during CAMP^{2}Ex for a cloud scene centered at [123.392°E, 15.2744°N] over the Philippine Sea at 02:10:06 UTC on 5 October, 2019. The arrows indicate the true north (green), flight direction (blue), and illumination (where the sunlight comes from, yellow). **(b)** Red channel radiance measured by the camera for the circular area indicated by the red circle in (a). Red squared region shows gridded radiance with a pixel size of 64x64 and spatial resolution of 100 m.

From the radiance field, we used both the traditional IPA (based on the IPA reflectance-to-COT mapping) and the new CNN to retrieve COT fields. Figure 11 shows the COT$_{IPA}$ and COT$_{CNN}$ fields, which are visually quite different. For relatively thin clouds (e.g., at around {2, 1.8}), the CNN tends to retrieve larger COT values than COT$_{IPA}$. Also, it returns more spatial structure than the IPA (e.g., around {2,-1}). To assess how either retrieval performs, we now apply the radiance self-consistency approach introduced with MODIS data in section 4.2. Using both the IPA and the CNN retrieval as input, we had EaR^{3}T calculate the (synthetic) radiance that the camera should have observed if the retrieval were accurate. The clouds are assumed to be located at 1-2 km. Such an assumption is inferred from low-level aircraft observations of clouds on the same day. These radiance fields are shown in Figure 12a and 12b, and can be compared to Figure 12c. Seven edge pixels have been removed from the original domain because the CNN performs poorly at edge pixels, and because the 3D calculations use periodic boundary conditions.
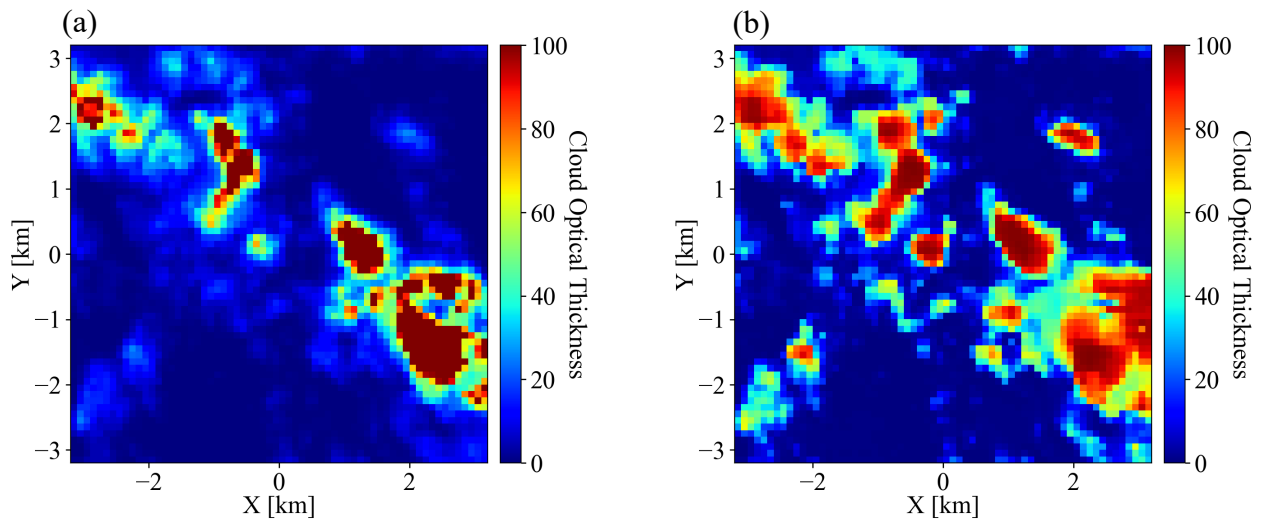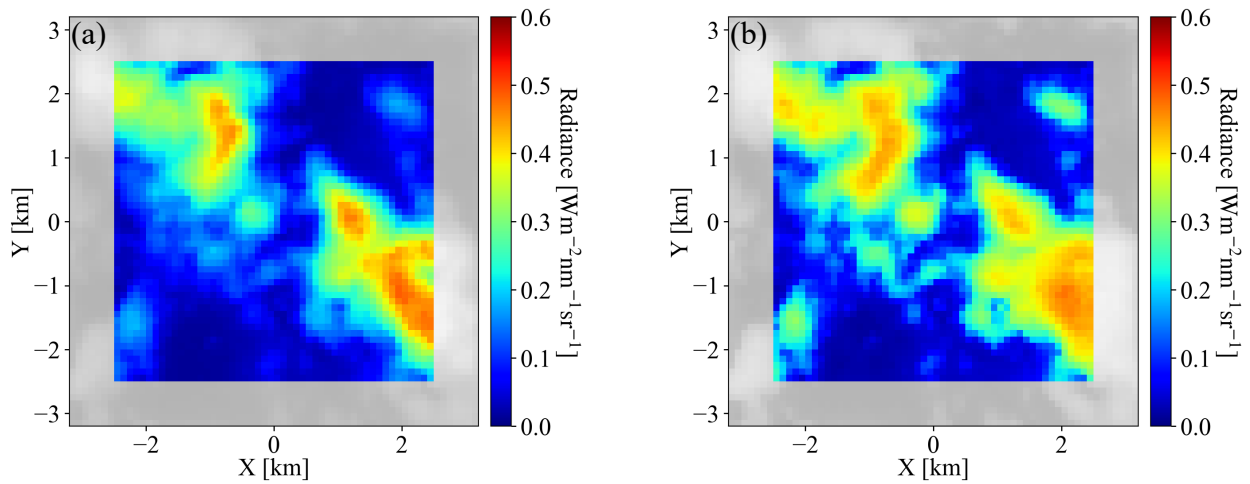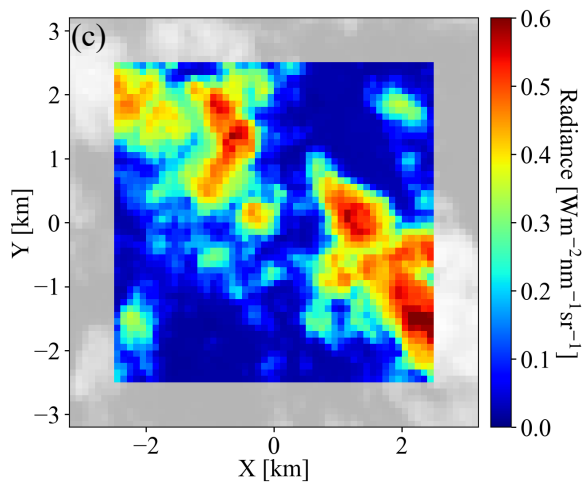
726

727 **Figure 11**. Cloud optical thickness for the gridded radiance in Figure 10b **(a)** estimated by IPA method and **(b)**
728   predicted by CNN.

729

730

731

732

733 **Figure 12**. 3D radiance calculations from EaR^{3}T at 600 nm based on cloud optical thickness field **(a)** estimated by
734   IPA, and **(b)** predicted by the CNN. The radiance measured by the all-sky camera (the same as Figure
735   10b) is provided in the same format at **(c)** for comparison. The calculations were originally performed
736   for the 64x64 domain. Then 7 pixels along each side of the domain (contoured in gray) were excluded,
737   which resulted in a 50x50 domain.
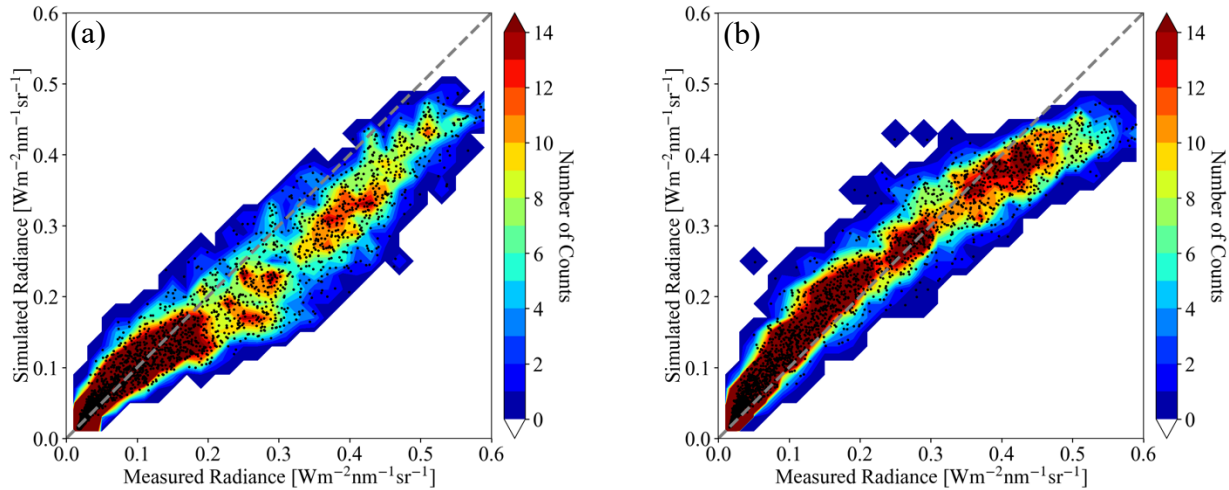
741 **Figure 13**. Scatter plot overlays 2D histogram of 3D radiance calculations at 600 nm based on cloud optical thickness
742   **(a)** estimated by IPA and **(b)** predicted by the CNN vs. measured red channel radiance from all-sky camera.

744   As evident from the brightest pixels in Figures 12b and 12c, the radiances simulated on the
745 basis of the COT$_{CNN}$ input are markedly lower than actually observed by the camera. This is
746 because the CNN was trained on a LES dataset with limited COT range that excluded the largest
747 COT that occurred in practice. This means that the observational data went beyond the original
748 training envelope of the CNN, which highlights the importance of choosing the CNN training data
749 carefully for a given region. In Figure 13, the simulations are directly compared with the original
750 observations, confirming that indeed the CNN-generated data are below the observations on the
751 high radiance end. Otherwise, the CNN-generated radiances agree with the observations. In
752 contrast, the IPA-generated data are high biased for the optically very thin clouds (radiance below
753 0.1) and systematically low-biased for the thick clouds (radiance above 0.2) when comparing with
754 the observations, over the dynamic range of the COT, which is indicative of the 3D retrieval bias
755 that we discussed earlier. A small high bias occurs in the COT$_{CNN}$ based radiance simulations for
756 the optically thin clouds (radiance value below 0.2). This probably because the CNN training as

757   described by Nataraja et al. (2022) is 1) based on a surface albedo of 0 and 2) aerosol-free

758   atmospheric environment (also aerosol-free setup for radiance simulations in Figure 13), where in

759   reality the ocean is slightly brighter and atmosphere is mixed with aerosols. Here again, the

760   radiance self-consistency approach proves useful despite the absence of ground truth data for the

761   COT. This is valuable because in reality satellite remote sensing does not have the ground truth of

762   COT, whereas radiance measurements are always available. For the CNN, the self-consistency of

763   the radiance is remarkable for most of the clouds (radiance smaller than 0.4), which encompass

764   86.8% of the total number of image pixels.

765   Finally, we use EaR^3T to propagate the 3D cloud retrieval bias into the associated bias in

766   estimating the cloud radiative effect from passive imagery retrievals, which means that we are

767   returning from a remote sensing to an energy perspective (irradiance) at the end of the paper. The

768   calculated cloud radiative effects (CRE) of both below-clouds (at the surface) and above-clouds

769   (at 2.5 km) are shown in Figure 14a and 14b. The most important histograms are those from 3D

770   irradiance calculations based on the CNN retrievals (gray solid line), as this combination would

771   be used in a next-generation framework for deriving CRE from passive remote sensing, and the

772   other would be IPA irradiance calculations based on the IPA retrieval (red solid line), as done in

773   the traditional (heritage) approach. The dashed lines are the other combinations. The mean values

774   (red vs. gray) indicate that in our case the traditional approach would lead to a high bias of more

775   than to 28% both at the surface and 20% above clouds due to low-biased COT_{IPA} (consistent with

776   findings of low-biased COT_{IPA}-derived reflectance from App. 1&2 and high-biased COT_{IPA}-

777   derived transmittance from App. 3). Here again, 3D biases do not cancel each other out in the

778   domain average. If the CNN had better fidelity even for optically thick clouds, the real bias in CRE

779   would be even larger. A minor, but interesting finding is that regardless of which COT retrieval is

780   used, the mean CRE is similar for IPA and 3D irradiance calculations (e.g., $\overline{CRE_{IPA}(COT_{CNN})} \approx$

781     $\overline{CRE_{3D}(COT_{CNN})}$, blue vertical dashed line locates near to gray vertical solid line), even though

782   the PDFs are different. By far the largest impact on accuracy comes from the retrieval technique,

783   not from the subsequent CRE calculations. Here again, the self-consistency check turns out as a

784   powerful metric to assess retrieval accuracy. Of course, we only used a single case in this part of

785   the paper. For future evaluation of the CNN versus the IPA, one would need to process larger

786   quantities of data in an automated fashion as done in the first part of the paper. This is beyond the

787   scope of this introductory paper, and will be included in future releases of EaR^3T and the CNN.

788
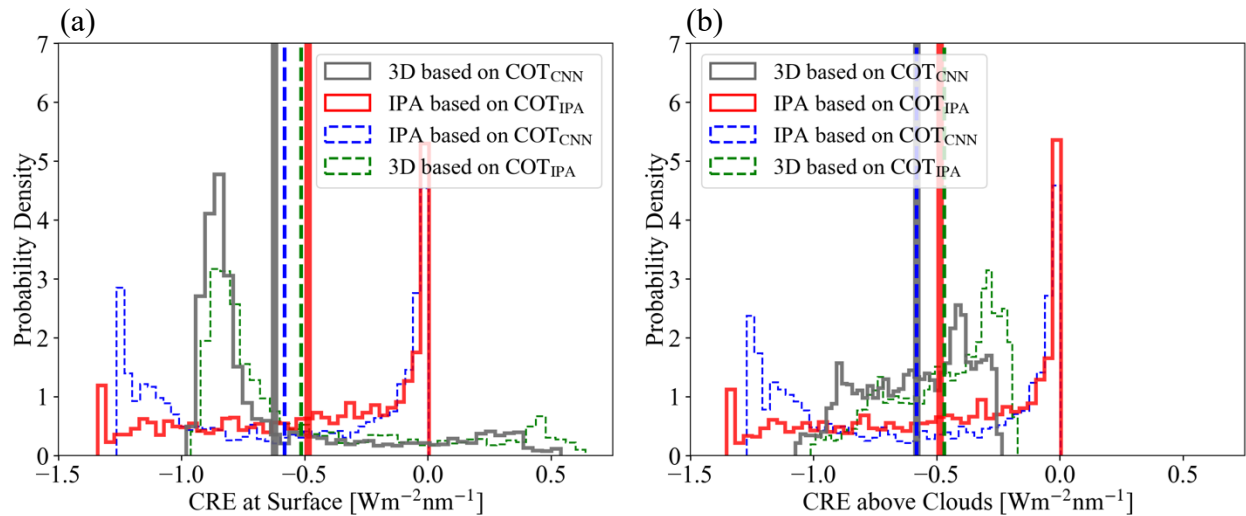
789

790 **Figure 14**. Histograms of cloud radiative effects derived from 1) 3D irradiance calculations based on COT_{CNN} (solid
791 gray), 2) IPA irradiance calculations based on COT_{IPA} (solid red), 3) IPA irradiance calculations based on
792 COT_{CNN} (dashed blue), and 4) 3D irradiance calculations based on COT_{IPA} (dashed green) both **(a)** at the
793 surface and **(b)** above the clouds. The mean values are indicated by vertical lines.

794

795 **7. Summary and Conclusion**

796 In this paper, we introduced EaR^{3}T, a toolbox that provides high-level interfaces to
797 automate and facilitate 1D- and 3D-RT calculations. We presented applications that used EaR^{3}T
798 to:

799   a) build a processing pipeline that can automatically simulate 3D radiance fields for satellite
800   instruments (currently OCO-2 and MODIS) from publicly available satellite surface and
801   cloud products at any given time over any specific region;

802   b) build a processing pipeline that can automatically simulate irradiance along all flight legs
803   of aircraft missions, based on geostationary cloud products;

804   c) simulate radiance and irradiance for high-resolution COT fields retrieved from an airborne
805   camera, using both a traditional 1D-RT (IPA) approach, and a newly developed 3D-RT
806   (CNN) approach that considers the spatial context of a pixel.

807 Unlike other satellite simulators that employ 1D-RT, EaR^{3}T is capable of performing the radiance
808 and irradiance calculations in 3D-RT mode. Optionally, it can be turned off to link back to
809 traditional 1D-RT codes, and to calculate 3D perturbations by considering the changes of 3D-RT
810 fields relative to the 1D-RT baseline.

811   With the processing pipeline under a) (App. 1 and App. 2, section 4), we prototyped a
812   3D-RT powered radiance loop (we call it "radiance self-consistency") that is envisioned for
813   upcoming satellite missions such as EarthCARE and AOS. Retrieved cloud fields (in our case,
814   from MODIS and from an airborne camera) are fed back into a 3D-RT simulation engine to
815   calculate at-sensor radiances, which are then compared with the original measurements. Beyond
816   currently included sensors, others can be added easily, taking advantage of the modular design of
817   EaR^{3}T. This radiance closure loop facilitates the evaluation of passive imagery products,
818   especially under spatially inhomogeneous cloud conditions. The automation of EaR^{3}T permits
819   calculations at any time and over any given region, and statistics can be built by looping over entire
820   orbits as necessary. The concept of radiance self-consistency could be valuable even for existing
821   imagery datasets because it allows the automated quantification of 3D-RT biases even without
822   ground truth such as airborne irradiance from suborbital activities. Also, it can be easily extended
823   to spectral or multi-angle observations as available from MODIS and MISR (Multi-Angle Imaging
824   Spectroradiometer), and thus providing more powerful constraints to the remote sensing products.
825   In the future it should be possible to include a 3D-RT pipeline such as EaR^{3}T into operational
826   processing of satellite derived data products.

827   Benefitting from the automation of EaR^{3}T in b) (App. 3, section 5), we performed 3D-RT
828   irradiance calculations for the entire CAMP^{2}Ex field campaign, moving well beyond radiation
829   closure case studies, and instead systematically evaluating satellite-derived radiation fields with
830   aircraft data for an entire region. From the comparison based on all below-cloud flight tracks
831   during the entire campaign, we found that the satellite-derived cloud transmittance was biased low
832   by 10% compared to the observations when relying on the heritage satellite cloud product.

833   From the statistical results of the CAMP^{2}Ex irradiance closure in b), we concluded that the
834   bias between satellite-derived irradiances and the ground truth from aircraft measurements was
835   due to a combination of the coarse spatial resolution of the geostationary imagery products and
836   3D-RT effects. To minimize the coarse-resolution part of the bias and thus to isolate the 3D-RT
837   bias, we used high-resolution airborne camera imagery in c) (App. 4, section 6), and found that
838   even with increased imager resolution, biases persisted. The at-sensor radiance derived from
839   COT$_{IPA}$ was inconsistent with the original measurements. For cloudy pixels, the calculated
840   radiance was well below the observations, confirming an overall low bias in COT$_{IPA}$. This low bias
841   could be largely mitigated with the context-aware CNN developed separately in Nataraja et al.

842 (2022) and included in EaR³T. Of course, this novel technique has limitations. For example, the

843 camera reflectance data went beyond the CNN training envelope, which would need to be extended

844 to larger COT in the future. In addition, the CNN only reproduces two-dimensional clouds fields

845 and does not provide access to the vertical dimension, which will be the next frontier to tackle.

846 Still, the greatly improved radiance consistency from COT_{IPA} to COT_{CNN} indicates that the EaR³T-

847 LES-CNN approach shows great promise for the mitigation of 3D-RT biases associated with

848 heritage cloud retrievals. We also discovered that for this particular case, the CRE calculated from

849 traditional 1D cloud products can introduce a warm bias of at least 28% at the surface and 20%

850 above clouds.

851   EaR³T has proven to be capable of facilitating 3D-RT calculations for both remote sensing

852 and radiative energy studies. Beyond the applications described in this paper, EaR³T has already

853 been extensively used by a series of on-going research projects such as producing massive 3D-RT

854 calculations as training data for a new generation of CNN models (Nataraja et al., 2022), evaluating

855 3D cloud radiative effects associated with aerosols (Gristey et al., 2022), creating flight track and

856 satellite track simulations for mission planning etc. More importantly, the strategies provided in

857 this paper put novel machine learning algorithms on a physical footing, opening the door for the

858 mitigation of complexity-induced biases in the near-future. More development effort will be

859 invested into EaR³T in the future, with the goals of minimizing the barriers to using 3D-RT

860 calculations, and to promote 3D cloud studies. EaR³T will continue to be an educational tool driven

861 by graduate students. In the future, we plan to add support for additional publicly available 3D RT

862 solvers, e.g., SHDOM (Spherical Harmonic Discrete Ordinate Method, Evans, 1998; Pincus and

863 Evans, 2009), as well as built-in support for HITRAN and associated correlated-k methods

864 (currently, we are implementing such an approach for the longwave wavelength range). From a

865 research perspective, we anticipate that EaR³T will enable the systematic quantification and

866 mitigation of 3D-RT biases of imagery-derived cloud-aerosol radiative effects, and may be the

867 starting point for operational use of 3D-RT for future satellite missions.

868

Appendix A

A1 - Technical Input and Output Parameters of EaR³T

EaR³T provides various functions that can be combined to tailored pipelines for automatic 3D radiative transfer (3D-RT) calculations as described in this paper (App. 1 – 5), as well as for complex research projects beyond. Since EaR³T is written in Python, the modules and functions can be integrated into existing functions developed by the users themselves. Parallelization is enabled in EaR³T by default through multi-processing to accelerate computations. If multiple CPUs are available, EaR³T will distribute jobs for the 3D RT calculations. By default, the maximum number of CPUs will be used. Since EaR³T is designed to make the process of setting up and running 3D-RT calculations simple, some parameters that are unavailable from the input data but are required by the RT solvers are populated via default values and assumptions. However, this does not mean that by using EaR³T, one must use these assumptions; they can be easily superseded by user-provided settings. To facilitate this process, Table A1 provides a detailed list of parameters (subject to change in future updates) that can be controlled and modified by the user. In `examples/02_modis_rad-sim.py`, we defined these user-controllable parameters as global variables for providing easy access to user. In the future, most of the parameters will be controllable through a dedicated configuration file for optimal transparency. These parameters can be changed within the code. For instance, by changing the parameters of `'date'` (Line 67 in `examples/02_modis_rad-sim.py`) and `'region'` (Line 68 in `examples/02_modis_rad-sim.py`) within `params` into the following:

```
params['date']   = datetime.datetime(2022, 2, 10)
params['region'] = [-6.8, -2.8, 17.0, 21.0]
```

one can perform similar RT calculations (as demonstrated in App. 2) for another date and region of interest (here, west Sahara Desert on 10 February, 2022). Note that the code is under active development, the line numbers are only valid in the version release of v0.1.1 and might change in the future. Given the input parameters, EaR³T will calculate radiance or irradiance and save the calculations into a HDF5 (Hierarchical Data Format version 5) file. The output data variables are provided in Table A2.

In addition to the example code, intuitive and simple examples are provided in `examples/00_er3t_mca.py` and `examples/00_er3t_lrt.py` for users who are interested in learning the basics of setting up EaR³T for calculations. At the current stage, only

900 limited documentation is provided. However, community support is available from the author of

901 this paper through Discord[6]. In the near-future, more effort will be invested into documentation to

902 give the user more autonomy in creating new applications that cannot be derived from those

903 provided in our paper.

904

Parameters	App. 1 examples/01_oc o2_rad-sim.py	App. 2 examples/02_mo dis_rad-sim.py	App. 3 examples/03_sp ns_flux-sim.py	App. 4 examples/04_ca m_nadir_rad-sim.py	App. 5 examples/05_cn n-les_rad-sim.py
Date	September 2, 2019 Specified at Line 66: `params['date']` And Line 1569: `date`	September 2, 2019 Specified at Line 68: `params['date']` And Line 1311: `date`	September 20, 2019 Specified at Line 439: `date` And Line 238: `date`	October 5, 2019 Specified at Line 59: `params['date']` And Line 215: `date`	October 5, 2019 Specified at Line 58: `params['date']` And Line 126: `date`
Geographical Region	Specified at Line 69: `params['region ']`	Specified at Line 69: `params['region ']`	Variable (depends on aircraft location)	N/A	N/A
Z Grid (Number of Grids/Resolut ion)	40 / 0.5 km Specified at Line 1476: `levels`	40 / 0.5 km Specified at Line 1220: `levels`	20 / 1 km Specified at Line 180: `levels`	40 / 0.5 km Specified at Line 174: `levels`	50 / 0.4km Specified at Line 92: `levels`
Wavelength	768.52 nm Specified at Line 67: `params['wavele ngth']`	650 nm Specified at Line 67: `params['wavele ngth']`	745 nm Specified at Line 440: `wavelength`	600 nm Specified at Line 58: `params['wavele ngth']`	600 nm Specified at Line 57: `params['wavele ngth']`
Atmospheric Gas Profile	US standard atmosphere Specified at Line 1479: `atm0`	US standard atmosphere Specified at Line 1223: `atm0`	US standard atmosphere Specified at Line 183: `atm0`	US standard atmosphere Specified at Line 177: `atm0`	US standard atmosphere Specified at Line 68: `params['atmosp heric_profile' ]` And Line 94: `atm0`
Atmospheric Gas Absorption	Case specific Specified at Line 1487: `abs0`	Default Absorption Database (Coddington et al., 2008) Specified at Line 1230: `abs0`	Default Absorption Database (Coddington et al., 2008) Specified at Line 189: `abs0`	Default Absorption Database (Coddington et al., 2008) Specified at Line 184: `abs0`	Default Absorption Database (Coddington et al., 2008) Specified at Line 97: `abs0`
Cloud Top Height (CTH)	From MODIS L2 cloud product Specified at Line 1520: `data['cth_2d']` And Line 1530: `cld0`	From MODIS L2 cloud product Specified at Line 1263: `data['cth_2d']` And Line 1273: `cld0`	From AHI L2 cloud product Specified at Line 208: `cth_2d` And Lines 212: `cld0`	2 km Specified at Line 63: `params['cloud_ top_height']` And Lines 199: `cld0`	From LES Specified at Line 103: `cld0`
Cloud Geometrical Thickness	1 km for CTH < 4 km; Variable that cloud base height is at 3 km for CTH > 4 km Specified at Line 1527: `cgt`	1 km for CTH < 4 km; Variable that cloud base height is at 3 km for CTH > 4 km And Line 1270: `cgt`	1 km Specified at Line 212: `cgt`	1 km Specified at Line 64: `params['cloud_ geometrical_th ickness']`	From LES Specified at Line 103: `cld0`

Cloud Optical Thickness	Used IPA reflectance-to-COT mapping for MODIS L1B Reflectance at 250 m resolution Specified at Line 1518: **data['cot_2d']** And Line 1530: **cld0**	Used IPA reflectance-to-COT mapping for MODIS L1B Reflectance at 250 m resolution Specified at Line 1261: **data['cot_2d']** And Line 1273: **cld0**	From AHI L2 cloud product Specified at Line 198: **cot_2d** And Lines 212: **cld0**	Used IPA reflectance-to-COT mapping and CNN for camera red channel radiance/reflectance at 100 m resolution Specified at Lines 474 and 493: **cot_2d** And Lines 199: **cld0**	From LES Specified at Line 103: **cld0**
Cloud Effective Radius	From MODIS L2 Cloud Product Specified at Line 1519: **data['cer_2d']** And Line 1530: **cld0**	From MODIS L2 Cloud Product Specified at Line 1262: **data['cer_2d']** And Line 1273: **cld0**	From AHI L2 cloud product Specified at Line 199: **cer_2d** And Lines 212: **cld0**	12 micron Specified at Lines 475 and 494: **cer_2d** And Lines 199: **cld0**	From LES Specified at Line 103: **cld0**
Scattering Phase Function	Mie (water cloud) Specified at Line 1536 **pha0** And Line 1573: **sca**	Mie (water cloud) Specified at Line 1279: **pha0** And Line 1315: **sca**	Mie (water cloud) Specified at Line 219: **pha0** And Line 237: **sca**	Mie (water cloud) Specified at Line 190: **pha0** And Line 219: **sca**	Mie (water cloud) Specified at Line 111: **pha0** And Line 130: **sca**
Surface Albedo	From MODIS surface albedo product and scaled by OCO-2 Specified at Line 1501: **mod43** And Line 1503: **sfc_2d**	From MODIS surface albedo product Specified at Line 1244: **mod43** And Line 1246: **sfc_2d**	0.03 Implicitly specified by default at Line 234: **mcarats_ng**	0.03 Specified at Line 61: **params['surface_albedo']** And Line 218: **surface_albedo**	0.03 Specified at Line 59: **params['surface_albedo']** And Line 133: **surface_albedo**
Solar Zenith Angle	From OCO-2 geolocation file Specified at Line 1554: **sza** And Line 1576: **solar_zenith_angle**	From MODIS geolocation file Specified at Line 1296: **sza** And Line 1318: **solar_zenith_angle**	Variable (depends on aircraft location and date and time)	28.90° Specified at Line 464: **geometry['sza']** And Line 222: **solar_zenith_angle**	29.16° Specified at Line 60: **params['solar_zenith_angle']** And Line 134: **solar_zenith_angle**
Solar Azimuth Angle	From OCO-2 geolocation file Specified at Line 1555: **saa** And Line 1577: **solar_azimuth_angle**	From MODIS geolocation file Specified at Line 1297: **saa** And Line 1319: **solar_azimuth_angle**	Variable (depends on aircraft location and date and time)	296.83° Specified at Line 465: **geometry['saa']** And Line 223: **solar_azimuth_angle**	296.83° Specified at Line 61: **params['solar_azimuth_angle']** And Line 135: **solar_azimuth_angle**
Sensor Altitude	705 km (satellite altitude) Implicitly specified by default at Line 1568: **mcarats_ng**	705 km (satellite altitude) Implicitly specified by default at Line 1310: **mcarats_ng**	N/A, three-dimensional irradiance outputs at user-defined Z grid	5.48 km (flight altitude) Specified at Line 466: **geometry['alt']** And Line 224: **sensor_altitude**	705 km (satellite altitude) Specified at Line 64: **params['sensor_altitude]** And Line 138: **sensor_altitude**
Sensor Zenith Angle	From OCO-2 geolocation file Specified at Line 1557: **vza**	From MODIS geolocation file Specified at Line 1302: **vza**	0° (nadir) Implicitly specified by default at Line 234: **mcarats_ng**	0° (nadir) Implicitly specified by default at Line 214: **mcarats_ng**	0° (nadir) Specified at Line 62: **params['sensor_zenith_angle']**

	And Line 1578: **sensor_zenith_angle**	And Line 1320: **sensor_zenith_angle**			And Line 136: **sensor_zenith_angle**
Sensor Azimuth Angle	From OCO-2 geolocation file Specified at Line 1558: **vaa** And Line 1579: **sensor_azimuth_angle**	From MODIS geolocation file Specified at Line 1303: **vaa** And Line 1321: **sensor_azimuth_angle**	0° (insignificant for nadir) Implicitly specified by default at Line 234: **mcarats_ng**	0° (insignificant for nadir) Implicitly specified by default at Line 214: **mcarats_ng**	0° (insignificant for nadir) Specified at Line 63: **params['sensor_azimuth_angle']** And Line 137: **sensor_azimuth_angle**
Number of Photons	1×10^8 per run Specified at Line 70: **params['photon']** And Line 1583: **photons**	1×10^8 per run Specified at Line 70: **params['photon']** And Line 1325: **photons**	1×10^7 per run Specified at Line 50: **params['photon']** And Line 243: **photons**	1×10^7 per run Specified at Line 60: **params['photon']** And Line 228: **photons**	1×10^8 per run Specified at Line 65: **params['photon']** And Line 141: **photons**
Number of Runs	3 Specified at Line 1581: **Nrun**	3 Specified at Line 1323: **Nrun**	3 Specified at Line 242: **Nrun**	3 Specified at Line 226: **Nrun**	3 Specified at Line 140: **Nrun**
Mode (3D or IPA)	3D and IPA Specified at Line 1704 and 1705: **solver** And Line 1584: **solver**	3D or IPA Specified at Line 1418: **solver** And Line 1326: **solver**	3D and IPA Specified at Lines 377 and 378: **solver** And Line 244: **solver**	3D Specified at Lines 507 and 508: **solver** And Line 229: **solver**	3D Specified at Line 143: **solver**
Parallelization Mode	Python multi-processing Specified at Line 1586: **mp_mode**	Python multi-processing Specified at Line 1328: **mp_mode**	Python multi-processing Specified at Line 247: **mp_mode**	Python multi-processing Specified at Line 231: **mp_mode**	Python multi-processing Specified at Line 145: **mp_mode**
Number of CPUs	12 Specified at Line 71: **params['Ncpu']** And Line 1585: **Ncpu**	12 Specified at Line 71: **params['Ncpu']** And Line 1327: **Ncpu**	12 Specified at Line 311: **Ncpu** And Line 246: **Ncpu**	12 Specified at Line 230: **Ncpu**	24 on clusters Specified at Line 144: **Ncpu**

905

Table A1: List of parameters used in the five applications. The line numbers used in the table are referring to the code script of each application. If two line numbers are provided, the first one indicates where the parameter is defined and the second one indicates where the parameter is passed into the radiative transfer setup. Users can change either one for customization purposes.

910

911

Metadata			
Variable Name	Description	Data Type	Dimension
mean/N_photon	Number of photons per run	Array	N_g
mean/N_run	Number of runs	Integer value	N/A
mean/toa	TOA downwelling flux	Float value	N/A
Radiance			
Variable Name	Description	Data Type	Dimension

Variable Name	Description	Data Type	Dimension
mean/rad	Radiance field at user specified altitude averaged over different runs	Array	(N_x, N_y)
mean/rad_std	Standard deviation of the radiance fields from different runs	Array	(N_x, N_y)
Irradiance			
Variable Name	Description	Data Type	Dimension
mean/f_down	Downwelling irradiance averaged over different runs	Array	(N_x, N_y, N_z)
mean/f_down_std	Standard deviation of the downwelling irradiance from different runs	Array	(N_x, N_y, N_z)
mean/f_down_diffuse	Diffuse downwelling irradiance averaged over different runs	Array	(N_x, N_y, N_z)
mean/f_down_diffuse_std	Standard deviation of the diffuse downwelling irradiance from different runs	Array	(N_x, N_y, N_z)
mean/f_down_direct	Direct downwelling irradiance averaged over different runs	Array	(N_x, N_y, N_z)
mean/f_down_direct_std	Standard deviation of the direct downwelling irradiance from different runs	Array	(N_x, N_y, N_z)
mean/f_up	Upwelling irradiance averaged over different runs	Array	(N_x, N_y, N_z)
mean/f_up_std	Standard deviation of the upwelling irradiance from different runs	Array	(N_x, N_y, N_z)

912

913 **Table A2**: Data variables contained in the output HDF5 file from EaR^{3}T for radiance and irradiance calculations. The
914 radiance is simulated with a user-specified sensor geometry at a given altitude using forward photon tracing.
915 The data variables listed under Metadata are included for both radiance and irradiance calculations. N_x,
916 N_y, and N_z are the number of pixels along x, y, and z direction, respectively. N_g is the number of g,
917 explained in Appendix A2 – Correlated-k.

918

919 **A2 – EaR^{3}T Code Walk-through**

920   We will provide a code walk-through of the OCO-2 and MODIS simulator applications
921 with the codes `examples/01_oco2_rad-sim.py` (App. 1) and
922 `examples/02_modis_rad-sim.py` (App. 2). The data acquisition (first step in Figure 1)

uses functions in `er3t/util`. App. 1 and App. 2 use the functions in `er3t/util/modis.py` and `er3t/util/oco2.py` for downloading the MODIS and OCO-2 data files from the respective NASA data archives and for processing the data (e.g., geo-mapping, gridding etc.). The user supplies minimum input (date and time, as well as latitudes and longitudes of the region of interest), which need to be specified in `satellite_download` (within the application codes). For example, for App. 1 and App. 2, the only user inputs are the date and time and the region of interest – in this case September 2, 2019, with the westernmost, easternmost, southernmost, and northernmost longitudes and latitudes of 109°W, 107°W, 37°N, and 39°N. In order for EaR³T to access any data archives such as NASA Earthdata, the user needs to create an account with them and store the credentials locally (detailed instructions are provided separately along with the EaR³T distribution).

After the data acquisition step, the satellite data are fed into the pre-processing step for 1) atmospheric gases (`er3t/pre/atm`), 2) clouds (`er3t/pre/cld`), 3) surface (`er3t/pre/sfc`) as shown in Figure 1. In the default configuration of the App. 1, the standard US atmosphere (Anderson et al., 1986; included in the EaR³T repository) is used within `atm`. EaR³T supports the input of user-specified atmospheric profiles, e.g., atmospheric profiles from reanalysis data for App. 2 as described in Chen et al. (2023), by making changes in `atm_atmmod` (from `er3t/pre/atm`). Subsequently, molecular scattering coefficients are calculated by `cal_mol_ext` (from `er3t/util`), and absorption coefficients for atmospheric gases are generated by (`er3t/pre/abs`). At the current development stage, two options are available:

1. Line-by-line (used by App. 1): The repository includes a sample file of absorption coefficient profiles for a subset of wavelengths within OCO-2's Oxygen A-Band channel, corresponding to a range of atmospheric transmittance values from low (opaque) to high (so-called "continuum" wavelength). They were generated by an external code (Chen et al., 2023) based on OCO-2's line-by-line absorption coefficient database (ABSCO, Payne et al., 2020). They are calculated for a fixed mixing ratio of 400 ppm. In a subsequent paper (Chen et al., 2023), an OCO-2 specific EaR³T code will be published where the actual mixing ratio is used. For each OCO-2 spectrometer wavelength within a given channel, hundreds of individual absorption coefficient profiles at the native resolution of ABSCO need to be considered across the instrument line shape (ILS, also known as the slit function) of the spectrometer. The ILS, as well as the incident solar irradiance, are also included in the file.

954   In subsequent steps, EaR³T performs RT calculations at the native spectral resolution of
955   ABSCO, but then combines the output by convolving with the ILS and outputs OCO-2
956   radiances or reflectances at the subset of wavelengths. For probabilistic (Monte Carlo) RT
957   solvers such as MCARaTS, the number of photons can be kept relatively low (e.g., 10^6
958   photons), and can be adjusted according to the values of the ILS at a particular ABSCO
959   wavelength. Any uncertainty at the ABSCO spectral resolution due to photon noise is greatly
960   reduced by convolving with the ILS for the final output.

961 2. Correlated-k (used by App. 2): This approach (Mlawer et al., 1997) is appropriate for
962   instruments such as MODIS with much coarser spectral resolution than OCO-2, as well as
963   for broadband calculations. In contrast to the line-by-line approach, RT calculations are not
964   performed at the native resolution of the absorption database, but at Gaussian quadrature
965   points (called "g's") that represent the full range of sorted absorption coefficients, and then
966   combined using Gaussian quadrature weights. The repository includes an absorption
967   database from Coddington et al. (2008), developed specifically for a radiometer with
968   moderate spectral resolution on the basis of HITRAN (high-resolution transmission
969   molecular absorption database) 2004 (Rothman et al., 2005). It was created for the ILS of
970   the airborne Solar Spectral Flux Radiometer (SSFR, Pilewskie et al., 2003), but is applied to
971   MODIS here, which has a moderate spectral resolution of 8-12 nm with 20-50 nm
972   bandwidths. It uses 16 absorption coefficient bins (g's) per target wavelength (this could
973   either be an individual SSFR or a MODIS channel), which are calculated by EaR³T with the
974   Coddington et al. (2008) database using the mixing ratios of atmospheric gases in the
975   previously ingested profile. In future implementations, the code will be updated to enable
976   flexible ILS and broadband calculations.

977   The `er3t/pre/cld` module calculates extinction, thermodynamic phase, and effective
978 droplet radius of clouds from the input data. The `er3t/pre/pha` module creates the required
979 single scattering albedo and scattering phase function. The default is a Henyey-Greenstein phase
980 function with a fixed asymmetry parameter of 0.85. Along with the current distribution (v0.1.1) of
981 EaR³T, the Mie phase functions based on thermodynamic phase, effective droplet radius, and
982 wavelength are supported. In this study, App. 1 and App. 2 use Mie phase functions calculated
983 from Legendre polynomial coefficients (originally distributed along with libRadtran) based on the
984 wavelength and cloud droplet effective radius. In the future, EaR³T will include stand-alone phase

985 functions, which can be chosen on the basis of droplet size distributions in addition to effective
986 radius. It is also possible to include aerosols in a similar fashion as clouds. This is done with the
987 `er3t/pre/aer` module. In the case of aerosols, spectral single scattering albedo and asymmetry
988 parameter are required as inputs in addition to the extinction fields.

989 After the optical properties are calculated, they are passed into the 3D-RT step
990 (`er3t/rtm/mca`). This step performs the setup of RT solver-specified input parameters and data
991 files, distributing runs over multiple Central Processing Units (CPUs), and post-processing RT
992 output files into a single, user-friendly HDF5 file. For example, when radiance is specified as
993 output (default in App. 1 and App. 2), key information such as the radiance field and its standard
994 deviation are stored in the final HDF5 file (details see Table 1).

995 While the EaR^{3}T repository comes with various applications such as App. 1 and App. 2,
996 described above, the functions used by these master or 'wrapper' programs can be organized in
997 different ways, where the existing applications serve as templates for a quick start when developing
998 new applications. The functions used by the master code pass information through the various
999 steps as Python objects. For example, in `examples/01_oco2_rad-sim.py`, the downloaded
1000 and processed satellite data are stored into the `sat` object. Later, the `sat` object is passed into an
1001 EaR^{3}T function to create the `cld` object that contains cloud optical properties. Similarly, EaR^{3}T
1002 provides functions to create the `atm`, and `sfc` objects with optical properties for atmospheric
1003 gases and the surface. These objects (`atm`, `cld`, `sfc`) are in turn passed on to solver-specific
1004 modules for performing RT calculations. The user can choose to save the data of the intermediate
1005 objects into Python pickle files after the first run. In this way, multiple calls with identical input
1006 can re-use existing data, which accelerates the processing time of EaR^{3}T. Unless the user specifies
1007 the `overwrite` keyword argument in the object call to reject saving pickle files, these shortcuts
1008 save significant time.

1009

1010 **Appendix B – App. 5 Radiance calculations based on the Large Eddy Simulation**

1011 The CNN COT retrieval framework was developed by Nataraja et al. (2022). It adapts a
1012 U-Net (Ronneberger et al., 2015) architecture and treats the retrieval of COT from radiance as a
1013 segmentation problem – probabilities of 36 COT classes (ranging from COT of 0 to 100) are
1014 returned as the final COT retrieved for a given cloud radiance field. It accounts for horizontal
1015 photon transport, which is neglected in traditional cloud retrieval algorithms; in other words, for

1016   the spatial context of cloudy pixels. It was trained on synthetic cloud fields generated by a Large

1017   Eddy Simulation (LES) model, which provides the ground truth of COT. Subsequently, EaR^{3}T was

1018   used to calculate 3D-RT radiances at 600 nm for LES cloud fields to establish a mapping between

1019   radiance to COT. Only six LES cases were used to represent the variability of the cloud

1020   morphology. Each of these fields are 480x480 pixels across (spatial resolution of 100 m). These

1021   large fields were mapped onto thousands of 64x64 mini tiles with spatial resolution of 100 m as

1022   described in Nataraja et al., 2022. To keep the training data set small, mini tiles selectively sampled

1023   according to their mean COT and standard deviation. This ensured an even representation of the

1024   dynamic range of COT and its variability, which was termed homogenization of the training data

1025   set. Figure A1 shows a collection of samples from the training data as an illustration. All the

1026   aforementioned simulation setup and techniques in data process are included in the App. 5 example

1027   code, which can be applied to the LES data (a different scene from the 6 scenes) distributed along

1028   with EaR^{3}T.

1029

1030
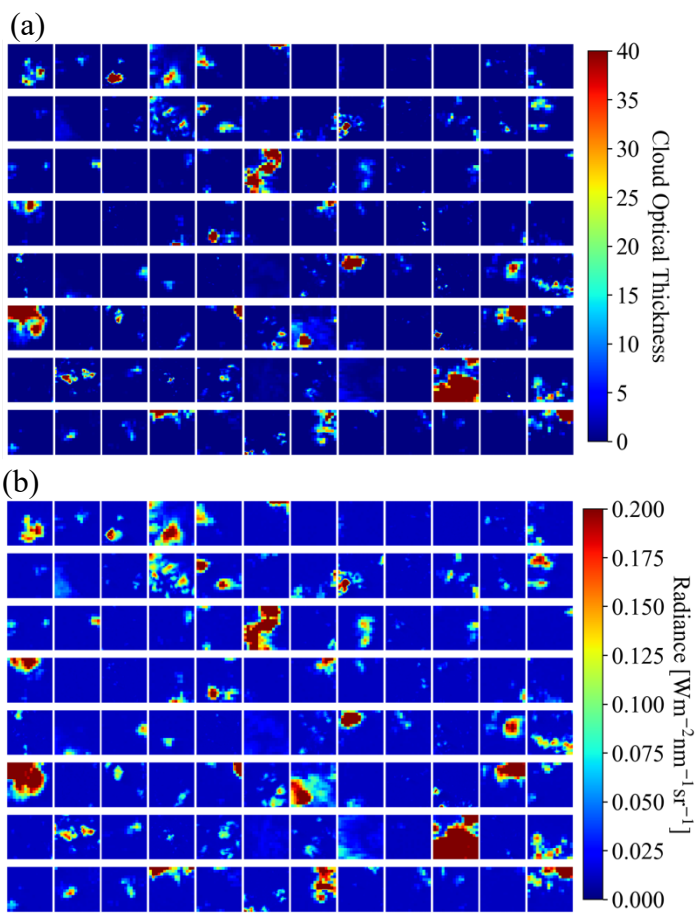
1031

1032   **Figure A1**. Illustrations of 64x64 tiles of **(a)** cloud optical thickness from LES data and **(b)** calculated 3D radiance at

1033   600 nm from EaR³T for CNN training.

1034

1035   **Appendix C**

1036   **C1. Cloud Detection/Identification**

1037   Cloudy pixels are identified through a thresholding method based on the red, green, and

1038   blue channels of MODIS. When the radiance values of the red, green, and blue channels of a pixel

1039   are all greater than a pre-calculated threshold value, the pixel is considered as cloudy, as illustrated

1040   by the following equation

1041 $$\text{If} \quad \begin{aligned} &Red > a_R \cdot Quantile(Red, q_0) \;\& \\ &Blue > a_B \cdot Quantile(Blue, q_0) \;\& \\ &Green > a_G \cdot Quantile(Green, q_0) \end{aligned} \quad \begin{cases} \textbf{Yes}: \text{cloudy} \\ \textbf{No}: \text{clear sky} \end{cases} \tag{A1}$$

1042   where a_R, a_B, and a_G are scale factors with a default value of 1.0, and $Quantile$ returns the q_0

1043   percentile of the sorted reflectance data (ascending order; $q_0 = 0.5$ is equivalent to the median).

1044   The scale factors can be adjusted separately to perform fine tuning for different surface types. For

1045   example, adjusting a_G will be more effective for separating clouds from greenish vegetation

1046   surface than the other two factors. For simplicity, they are all set to 1.0 for the case shown in App.

1047   1 and 2. The q_0 is determined by the following equation,

1048 $$q_0 = \max(0, \quad 1 - frac_{cld} \cdot 1.2) \tag{A2}$$

1049   where $frac_{cld}$ is cloud fraction obtained from the MODIS L2 cloud product (number of cloudy

1050   pixels divided by the number of total pixels). Through the definition of q_0, the threshold-based

1051   cloud detection method is pegged to the MODIS product at the domain scale. Because of the coarse

1052   resolution of the MODIS-based cloud mask, it cannot be used directly for our application.

1053   However, it uses many more channels than available at high spatial resolution, and is therefore

1054   more accurate. The factor of 1.2 can be adjusted. A value of higher than 1 allows for clouds that

1055   are not detected by MODIS (for various reasons, for example because of their spatial scale) to be

1056   picked up. At the same time, this leads to over-detection (false positives, i.e. clear-sky pixels

1057   identified as cloudy), and therefore the thresholding is only the first step (primary thresholding),

1058   followed by the next (secondary) step where false positives are removed.

1059   The secondary step is based on MODIS L2 cloud products: *COT* (cloud optical thickness),

1060   *CER* (cloud effective radius), and *CTH* (cloud top height). For the pixels that are identified as

1061   cloudy in the primary thresholding, especially at the lower end of the reflectance (*Ref.*), we rely

1062 on the clear-sky identifiers from MODIS L2 cloud product (where no cloud products are retrieved),

1063 as illustrated by the following equation

1064 $\textbf{If} \quad \begin{matrix} Ref. < Median(Ref.) \ \& \\ COT, CER, and \ CTH \ are \ NaN \end{matrix} \begin{cases} \textbf{Yes}: \text{clear sky} \\ \textbf{No}: \text{cloudy} \end{cases}$ (A3)

1065 Figure A2 shows the cloud mask from primary thresholding (Equation A1, red and purple), and

1066 the pixels that are reverted to clear-sky by the secondary filter (Equation A2, red).

1067
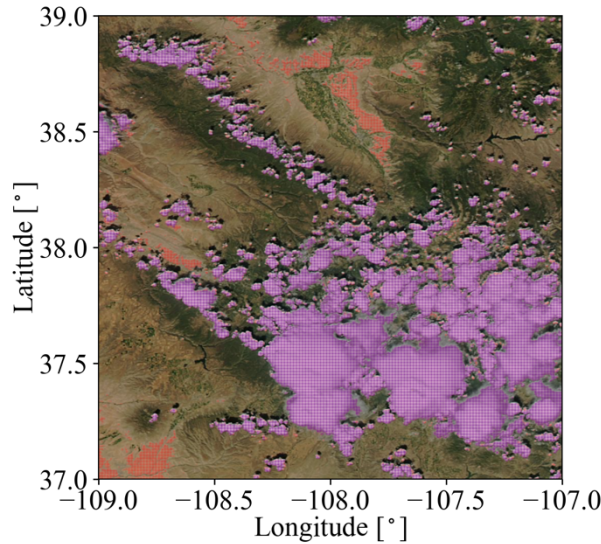
1068

1069 **Figure A2**. Cloud mask for the scene shown in Figure 2. Red and purple indicate pixels identified as cloudy through

1070 the primary thresholding (Equation A1) and purple indicates pixels finally identified as cloudy after applying

1071 secondary filter (Equation A3).

1072

1073 **C2. IPA Reflectance-to-COT Mapping**

1074 In order to retrieve COT (cloud optical thickness) from cloud reflectance as measured by

1075 various instruments, we use the EaR^{3}T built-in solver MCARaTS in IPA mode to calculate a

1076 lookup table of reflectance as a function of COT. The function for generating these lookup tables

1077 is included in EaR^{3}T as `er3t.rtm.mca.func_ref_vs_cot`. Two mappings are generated

1078 for App. 1&2 to account for geometrically thin (cloud top height less than 4 km) and thick (cloud

1079 top height greater than 4 km) clouds separately while a single mapping is generated for App. 4.

1080 Specifically, for a range of COT (0 to 200), reflectance is calculated from EaR^{3}T with the same

1081 input parameters (wavelength, viewing and solar geometries, and surface albedo) listed in Table

1082 A1 for each application except for a few simplifications described in the following table (Table

1083 A3):

1084

|	App. 1 & 2		App. 4
Cloud Type	Geometrically Thin Clouds	Geometrically Thick Clouds	All
Cloud Effective Radius	$10 \ \mu m$	$20 \ \mu m$	$10 \ \mu m$
Cloud Top Height	3 km	10 km	2 km
Cloud Geometrical Thickness	1 km	7 km	1 km
Surface Albedo	0.08 (domain average of the MCD43 WSA)	0.08 (domain average of the MCD43 WSA)	0.03

1085

1086 **Table A3**: List of parameters for deriving IPA reflectance-to-COT (cloud optical thickness) mappings for App. 1&2
1087 and App. 4 in addition to Table A1.

1088

1089 The clouds are assumed horizontally homogeneous over a 2×2 pixel domain. For each
1090 calculation, 10^8 photons are used for running EaR^{3}T in IPA mode. After calculating $R(COT)$, the
1091 inverse relationship of $COT(R)$ is then used for estimating COT at any given R for the cloudy
1092 pixels. Figure A3 shows the IPA reflectance-to-COT mappings created for App. 1&2, and App 4.
1093 Note that the difference between the App. 1&2 thin clouds (blue) and App. 4 (green) is due to
1094 different surface albedos (when COT less than 20) and sensor viewing geometries (when COT
1095 greater than 20, specified in Table A1). Note that this approach will ensure IPA
1096 radiance/reflectance consistency (retrieved IPA COT will reproduce the exact IPA cloud
1097 reflectance, see Figure A4) because the radiative transfer processes of $R(COT)$ and $COT(R)$ are
1098 the same. However, since it makes some simplifications as mentioned above, uncertainties are
1099 expected for a complicated atmospheric environment (varying cloud thermodynamic phase,
1100 effective radius, cloud top height, geometrical thickness, vertical profile; variable surface albedo
1101 and topography), which are shown up as spread (deviations from identity line) in Figure A4.

1102
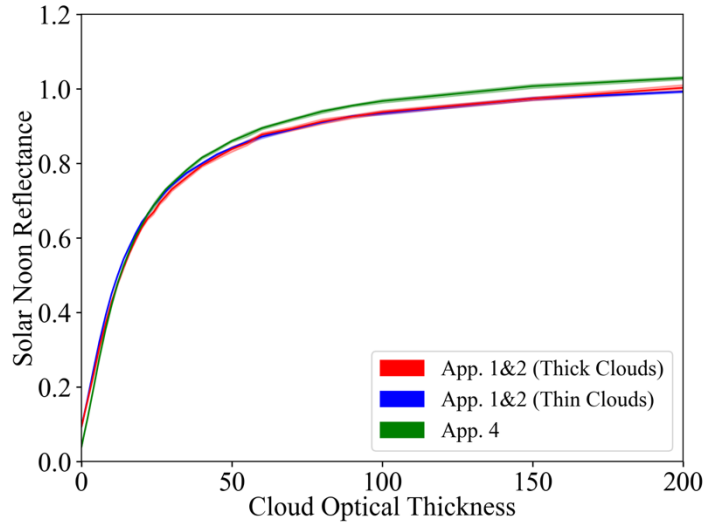
Figure A3. The IPA reflectance-to-COT mappings used for App. 1&2 (red and blue) and App. 4 (green). The reflectance is normalized by the cosine of solar zenith angle (referred to as solar noon reflectance). The uncertainties associated with photon statistics are indicated by the shaded area.
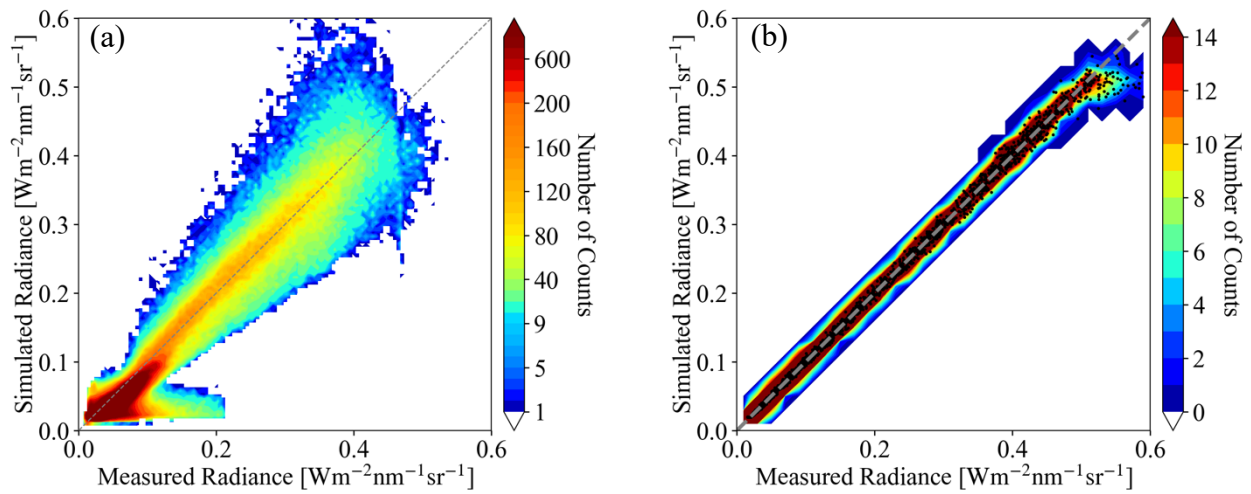
Figure A4. (a) and **(b)** are the same as Figure 7 and Figure 13b except for the IPA radiance calculations.

Appendix D

D1. Parallax Correction

From the satellite's view, the clouds (especially high clouds) will be placed at inaccurate locations on the surface, which have shifted from their actual locations due to the parallax effect. We followed simple trigonometry to correct for it, as follows:

Longitude correction (positive from west to east):

1118 $$\delta lon = \frac{\left(z_{cld} - z_{sfc}\right) \cdot \tan(\theta) \cdot \sin(\phi)}{\pi \cdot R_{Earth}} \times 180° \tag{A4}$$

1119 Latitude correction (positive from south to north):

1120 $$\delta lat = \frac{\left(z_{cld} - z_{sfc}\right) \cdot \tan(\theta) \cdot \cos(\phi)}{\pi \cdot R_{Earth}} \times 180° \tag{A5}$$

1121 where $(lon_{sat}, lat_{sat}, z_{sat})$ is the satellite location and θ and ϕ (0º at north, positive clockwise)

1122 are the sensor viewing zenith and azimuth angles. z_{cld} and z_{sfc} are the cloud top height and the

1123 surface height. R_{Earth} is the radius of the Earth. Figure A2 shows an illustration of the parallax

1124 correction for the cloud field in the inset in Figure 2. Note that discontinuities in the latitude and

1125 longitude fields arising from different combinations of sensor viewing geometries and cloud top

1126 and surface heights may lead to gaps in the cloud fields. These gaps are identified and filled in

1127 with the average of data from adjacent pixels (plus minus two pixels along x and y) through the

1128 following process:

1129 **If** $\begin{matrix} pixel_{ij}^{aft} \text{ is clear } \& \text{ } pixel_{ij}^{bef} \text{ is cloudy } \& \\ cldfrac(pixel^{bef}[i-2:i+2, j-2:j+2]) > frac_a \& \\ cldfrac(pixel^{aft}[i-2:i+2, j-2:j+2]) > frac_b \& \end{matrix}$ $\begin{cases} \textbf{Yes: } \text{fill } pixel_{ij}^{aft} \text{ with the average of} \\ cld(pixel^{aft}[i-2:i+2, j-2:j+2]) \end{cases}$

1130 where $pixel_{ij}$ indicates the pixel at i along x and j along y, bef and aft refer to before and after

1131 parallax correction respectively, $cldfrac$ calculates cloud fraction (number of cloudy pixels

1132 divided by total pixel number), and cld selects data where pixels are identified as cloudy. The

1133 $frac_a$ and $frac_b$ are set to 0.7 for the cases demonstrated in the paper. Lower $frac_a$ tends to over

1134 select clear-sky pixels at the cloud edge and lower $frac_b$ tends to over correct clear-sky pixels

1135 within clouds that are not clear-sky due to parallax artifacts. While increase $frac_a$ and $frac_b$

1136 tends to under correct parallax artifacts.

1137

1138 **D2. Wind Correction**

1139 The wind correction aims at correcting the movement of clouds when advected by the wind

1140 between two different satellites' overpasses.

1141 Longitude correction (positive from west to east):

1142 $$\delta lon = \frac{\bar{u} \cdot \delta t}{\pi \cdot R_{Earth}} \times 180° \tag{A6}$$

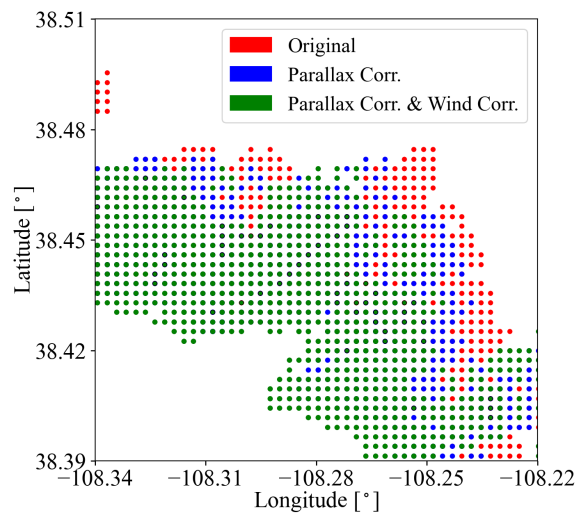1143 Latitude correction (positive from south to north):

$$\delta lat = \frac{\bar{v} \cdot \delta t}{\pi \cdot R_{Earth}} \times 180° \tag{A7}$$

where $\bar{u}$ and $\bar{v}$ are the domain-averaged 10 m zonal and meridional wind speeds, and δt is the time difference between two different satellites that fly on the same orbit. Figure A2 shows the cloud location after applying the parallax (Appendix D1) and wind correction for the cloud field in the inset from Figure 2.

Figure A5. An illustration of correcting cloud location (red) for parallax effect (blue) and wind effect (green) for the cloud field of the inset in Figure 2. Filled cloud gaps as described in Appendix D1 are indicated by black circles.

Data availability

For App. 1 and App. 2, the OCO-2 data were provided by the NASA Goddard Earth Sciences Data and Information Services Center (GES DISC, https://oco2.gesdisc.eosdis.nasa.gov/data) and the MODIS data were provided by the NASA Goddard Space Flight Center's Level-1 and Atmosphere Archive and Distribution System (LAADS, https://ladsweb.modaps.eosdis.nasa.gov/archive), which are all publicly available and can be downloaded by EaR^{3}T through the application code. For App. 3, the AHI data were processed by Holz's (coauthor of this paper) team. The SPN-S data were provided by Schmidt and Norgren (coauthors of this paper). Both the AHI and SPN-S data are publicly available at NASA Airborne Science Data for Atmospheric Composition (https://www-air.larc.nasa.gov/missions/camp2ex/index.html). The AHI data and the SPN-S data for the flight track indicated in Figure 8 of the paper are distributed along with EaR^{3}T for demonstration purpose. For App. 4, all sky camera imagery and CNN model are distributed along with EaR^{3}T. EaR^{3}T is publicly available and can be accessed and downloaded at https://github.com/hong-chen/er3t (or https://doi.org/10.5281/zenodo.7734965 for v0.1.1 used in this paper; Chen and Schmidt, 2022).

Author contributions

All the authors helped with editing the paper. HC developed the EaR^{3}T package in Python including the application code, performed the analysis, and wrote the majority of the paper with input from the other authors. KSS provided an initial MCARaTS simulation wrapper code in Interactive Data Language (IDL); helped with the structure design of EaR^{3}T; and helped with interpreting the results and writing the paper. SM helped with the OCO-2 data interpretation. VN trained and provided the CNN model. MN helped with the SPN-S instrument calibration and data processing. JG and GF helped with testing EaR^{3}T and the LES data interpretation. RH provided the AHI data and helped with the data interpretation. HI helped with the implementation of MCARaTS in EaR^{3}T.

References

Anderson, G. P., Clough, S. A., Kneizys, F. X., Chetwynd, J. H., and Shettle, E. P.: AFGL atmospheric constituent profiles (0–120 km), Tech. Rep. AFGL-TR-86–0110, Air Force Geophys. Lab., Hanscom Air Force Base, Bedford, Massachusetts, U.S.A., 1986.

Barker, H. and Liu, D.: Inferring optical depth of broken clouds from Landsat data, J. Climate, 8, 2620–2630, 1995.

Barker, H. W., Jerg, M. P., Wehr, T., Kato, S., Donovan, D. P., and Hogan, R. J.: A 3D cloud construction algorithm for the EarthCARE satellite mission, Q. J. Roy. Meteor. Soc., 137, 1042– 1058, https://doi.org/10.1002/qj.824, 2011.

Barker, H. W., Kato, S., and Wehr, T.: Computation of solar radiative fluxes by 1-D and 3-D methods using cloudy atmospheres inferred from A-train satellite data, Surv. Geophys., 33, 657–676, 2012.

Cahalan, R., Oreopoulos, L., Marshak, A., Evans, F., Davis, A., Pincus, R., Yetzen, K. H., Mayer, B., Yetzer, K. H., Mayer, B., Davies, R., Ackerman, T. P., Barker, H. W., Clothiaux, E. E., Ellingson, R. G., Garay, M. J., Kassianov, E., Kinne, S., Macke, A., O'Hirok, W., Partain, P. T., Prigarin, S. M., Rublev, A. N., Stephens, G. L., Szczap, F., Takara, E. E., Varnai, T., Wen, G., and Zhuravleva, T.: The I3RC: Bringing Together the Most Advanced Radiative Transfer Tools for Cloudy Atmospheres, B. Am. Meteorol. Soc., 86, 1275–1293, 2005.

Chen, H. and Schmidt, S.: er3t-v0.1.1, https://doi.org/10.5281/zenodo.7734965, 2023.

Chen, H., Schmidt, S., and Holz, R. E.: Synchronized Flight Videos for NASA CAMP[2]Ex, https://doi.org/10.5281/zenodo.7358509, 2022.

Chen, Y.-W., Schmidt, S., Massie, S., Chen, H., Crisp, D., Kulawik, S., Merrelli, A., McDuffie, J., Iwabuchi, H.: Uncovering the Mechanism for Trace Gas Spectroscopy Biases in the Vicinity of Clouds With the OCO-2 3D Radiative Transfer Satellite Radiance Simulator, Atmos. Meas. Tech., *in prep.*, 2023.

Crisp, D.: Measuring Atmospheric Carbon Dioxide from Space with the Orbiting Carbon Observatory-2 (OCO-2), P. Soc. Photo.-Opt. Ins., 9607, 960702, https://doi.org/10.1117/12.2187291, 2015.

Coddington, O., Schmidt, K. S., Pilewskie, P., Gore, W. J., Bergstrom, R., Roman, M., Redemann, J., Russell, P. B., Liu, J., and Schaaf, C. C.: Aircraft measurements of spectral surface albedo and its consistency with ground-based and space-borne observations, J. Geophys. Res., 113,

1219   D17209, doi:10.1029/2008JD010089, 2008.

1220   Deneke, H., Barrientos-Velasco, C., Bley, S., Hünerbein, A., Lenk, S., Macke, A., Meirink, J. F.,
1221   Schroedter-Homscheidt, M., Senf, F., Wang, P., Werner, F., and Witthuhn, J.: Increasing the
1222   spatial resolution of cloud property retrievals from Meteosat SEVIRI by use of its high-
1223   resolution visible channel: implementation and examples, Atmos. Meas. Tech., 14, 5107–
1224   5126, https://doi.org/10.5194/amt-14-5107-2021, 2021.

1225   Deutschmann, T., Beirle, S., Friess, U., Grzegorski, M., Kern, C., Kritten, L., Platt, U., Prados-
1226   Roman, C., Pukite, J., Wagner, T., Werner, B., and Pfeilsticker, K.: The Monte Carlo
1227   atmospheric radiative transfer model McArtim: introduction and validation of Jacobians and
1228   3-D features, J. Quant. Spectrosc. Ra., 112(6), 1119–1137, ISSN 0022-4073,
1229   doi:10.1016/j.jqsrt.2010.12.009, 2011.

1230   Doicu, A., Efremenko, D., and Trautmann, T.: A multi-dimensional vector spherical harmonics
1231   discrete ordinate method for atmospheric radiative transfer, J. Quant. Spectrosc. Ra., 118,
1232   121–131, https://doi.org/10.1016/j.jqsrt.2012.12.009, 2013.

1233   Emde, C., Barlakas, V., Cornet, C., Evans, F., Korkin, S., Ota, Y., Labonnote, L. C., Lyapustin,
1234   A., Macke, A., Mayer, B., and Wendisch, M.: IPRT polarized radiative transfer model
1235   intercomparison project – Phase A, Journal of Quantitative Spectroscopy and Radiative
1236   Transfer, 164, 8–36, https://doi.org/10.1016/j.jqsrt.2015.05.007, 2015.

1237   Emde, C., Buras-Schnell, R., Kylling, A., Mayer, B., Gasteiger, J., Hamann, U., Kylling, J., Richter,
1238   B., Pause, C., Dowling, T., and Bugliaro, L.: The libRadtran software package for radiative
1239   transfer calculations (version 2.0.1), Geosci. Model Dev., 9, 1647–1672,
1240   https://doi.org/10.5194/gmd-9-1647-2016, 2016.

1241   Evans, K. F.: The spherical harmonics discrete ordinate method for three-dimensional atmospheric
1242   radiative transfer, J. Atmos. Sci., 55, 429–446, 1998.

1243   Gatebe, C. K., Jethva, H., Gautam, R., Poudyal, R., and Várnai, T.: A new measurement approach
1244   for validating satellite-based above-cloud aerosol optical depth, Atmos. Meas. Tech., 14,
1245   1405–1423, https://doi.org/10.5194/amt-14-1405-2021, 2021.

1246   Gristey, J. J., Feingold, G., Glenn, I. B., Schmidt, K. S., and Chen, H.: Surface Solar Irradiance in
1247   Continental Shallow Cumulus Fields: Observations and Large-Eddy Simulation, J. Atmos.
1248   Sci., 77, 1065–1080, https://doi.org/10.1175/JAS-D-19-0261.1, 2020a.

1249   Gristey, J. J., Feingold, G., Glenn, I. B., Schmidt, K. S., and Chen, H.: On the Relationship

Between Shallow Cumulus Cloud Field Properties and Surface Solar Irradiance, Geophysical Research Letters, 47, e2020GL090152, https://doi.org/10.1029/2020GL090152, 2020b.

Gristey, J. J., Feingold, G., Glenn, I. B., Schmidt, K. S., and Chen, H.: Influence of Aerosol Embedded in Shallow Cumulus Cloud Fields on the Surface Solar Irradiance, Journal of Geophysical Research: Atmospheres, 127, e2022JD036822, https://doi.org/10.1029/2022JD036822, 2022.

Heidinger, A. K., Foster, M. J., Walther, A., and Zhao, X.: The Pathfinder Atmospheres-Extended AVHRR climate dataset, B. Am. Meteorol. Soc., 95, 909–922, https://doi.org/10.1175/BAMS-D-12-00246.1, 2014.

Illingworth, A. J., Barker, H. W., Beljaars, A., Chepfer, H., Delanoe, J., Domenech, C., Donovan, D. P., Fukuda, S., Hirakata, M., Hogan, R. J., Huenerbein, A., Kollias, P., Kubota, T., Nakajima, T., Nakajima, T. Y., Nishizawa, T., Ohno, Y., Okamoto, H., Oki, R., Sato, K., Satoh, M., Wandinger, U., Wehr, T., and van Zadelhoff, G.: The EarthCARE Satellite: the next step forward in global measurements of clouds, aerosols, precipitation and radiation, B. Am. Meteorol. Soc, 96, 1311–1332, https://doi.org/10.1175/BAMS-D-12-00227.1, 2015.

Iwabuchi, H.: Efficient Monte Carlo methods for radiative transfer modeling, J. Atmos. Sci., 63, 2324–2339, 2006.

Kindel, B. C., Schmidt, K. S., Pilewskie, P., Baum, B. A., Yang, P., and Platnick, S.: Observations and modeling of ice cloud shortwave spectral albedo during the Tropical Composition, Cloud and Climate Coupling Experiment (TC[4]), J. Geophys. Res., 115, D00J18, doi:10.1029/2009JD013127, 2010.

King, M., and Platnick, S.: The Earth Observing System (EOS), Comprehensive Remote Sensing, 7, 26, doi:10.1016/b978-0-12-409548-9.10312-4, 2018.

Levis, A., Schechner, Y. Y., Davis, A. B., and Loveridge, J.: Multi-View Polarimetric Scattering Cloud Tomography and Retrieval of Droplet Size, Remote Sens., 12, 2831, https://doi.org/10.3390/rs12172831, 2020.

Li, J., Scinocca, J., Lazare, M., McFarlane, N., von Salzen, K., and Solheim, L.: Ocean Surface Albedo and Its Impact on Radiation Balance in Climate Models, J. Climate, 19, 6314–6333, 2006.

Long, C. N., Bucholtz, A., Jonsson, H., Schmid, B., Vogelmann, A., and Wood, J.: A Method of Correcting for Tilt from Horizontal in Downwelling Shortwave Irradiance Measurements on

Moving Platforms, The Open Atmospheric Science Journal, 4, 78–87, 2010.

Loveridge, J., Levis, A., Di Girolamo, L., Holodovsky, V., Forster, L., Davis, A. B., and Schechner, Y. Y.: Retrieving 3D distributions of atmospheric particles using Atmospheric Tomography with 3D Radiative Transfer – Part 1: Model description and Jacobian calculation, Atmos. Meas. Tech. Discuss. [preprint], https://doi.org/10.5194/amt-2022-251, in review, 2022.

Masuda, R., Iwabuchi, H., Schmidt, K. S., Damiani, A. and Kudo, R.: Retrieval of Cloud Optical Thickness from Sky-View Camera Images using a Deep Convolutional Neural Network based on Three-Dimensional Radiative Transfer, Remote Sensing, 11(17), 1962, doi:10.3390/rs11171962, 2019.

Marshak, A., Davis, A., Wiscombe, W., and Cahalan, R.: Radiative smoothing in fractal clouds, J. Geophys. Res., 100, 26247–26261, https://doi.org/10.1029/95JD02895, 1995.

Marshak, A., Wen, G., Coakley, J., Remer, L., Loeb, N. G., and Cahalan, R. F.: A simple model for the cloud adjacency effect and the apparent bluing of aerosols near clouds, J. Geophys. Res., 113, D14S17, https://doi.org/10.1029/2007JD009196, 2008.

Massie, S. T., Schmidt, K. S., Eldering, A., and Crisp, D.: Observational evidence of 3-D cloud effects in OCO-2 CO2 retrievals, J. Geophys. Res. Atmos., 122, 7064–7085, https://doi.org/10.1002/2016JD026111, 2017.

Mayer, B. and Kylling, A.: Technical note: The libRadtran software package for radiative transfer calculations – description and examples of use, Atmos. Chem. Phys., 5, 1855–1877, https://doi.org/10.5194/acp-5-1855-2005, 2005.

Mayer, B.: Radiative transfer in the cloudy atmosphere, EPJ Web of Conferences, 1, 75–99, doi:10.1140/epjconf/e2009-00912-1, 2009.

Mlawer, E. J., Taubman, S. J., Brown, P. D., Iacono, M. J., and Clough, S. A.: Radiative transfer for inhomogeneous atmospheres: RRTM, a validated correlated-k model for the longwave, J. Geophys. Res., 102, 16663–16682, 1997.

Nakajima, T. and King, M. D.: Determination of the optical thickness and effective particle radius of clouds from reflected solar radiation measurements. Part I: Theory, J. Atmos. Sci., 47, 1878–1893, 1990.

Nataraja, V., Schmidt, S., Chen, H., Yamaguchi, T., Kazil, J., Feingold, G., Wolf, K., and Iwabuchi, H.: Segmentation-Based Multi-Pixel Cloud Optical Thickness Retrieval Using a Convolutional Neural Network, Atmos. Meas. Tech., 15, 5181–5205, doi:10.5194/amt-15-

5181-2022, 2022.

Norgren, M. S., Wood, J., Schmidt, K. S., van Diedenhoven, B., Stamnes, S. A., Ziemba, L. D., Crosbie, E. C., Shook, M. A., Kittelman, A. S., LeBlanc, S. E., Broccardo, S., Freitag, S., and Reid, J. S.: Above-aircraft cirrus cloud and aerosol optical depth from hyperspectral irradiances measured by a total-diffuse radiometer, Atmos. Meas. Tech., 15, 1373–1394, https://doi.org/10.5194/amt-15-1373-2022, 2022.

Payne, V. H., Drouin, B. J., Oyafuso, F., Kuai, L., Fisher, B. M., Sung, K., Nemchicka, D., Crawford, T. J., Smyth, M., Crisp, D., Adkins, E., Hodges, J. T., Long, D. A., Mlawer, E. J., Merrelli, A., Lunny, E., and O'Dell, C. W.: Absorption coefficient (ABSCO) tables for the Orbiting Carbon Observatories: version 5.1, J. Quant. Spectrosc. Ra., 255, 1–16, https://doi.org/10.1016/j.jqsrt.2020.107217, 2020.

Pilewskie, P., Pommier, J., Bergstrom, R., Gore, W., Howard, S., Rabbette, M., Schmid, B., Hobbs, P. V., and Tsay, S. C.: Solar spectral radiative forcing during the Southern African Regional Science Initiative, J. Geophys. Res., 108, 8486, https://doi.org/10.1029/2002JD002411, 2003.

Pincus, R. and Evans, K. F.: Computational cost and accuracy in calculating three-dimensional radiative transfer: Results for new implementations of Monte Carlo and SHDOM, J. Atmos. Sci., 66, 3131–3146, 2009.

Platnick, S., King, M. D., Ackerman, S. A., Menzel, W. P., Baum, B. A., Riédi, J. C., and Frey, R. A.: The MODIS cloud products: Algorithms and examples from Terra, IEEE T. Geosci. Remote, 41, 459–473, 2003.

Reid, J. S., Maring, H. B., Narisma, G. T., van den Heever, S., Di Girolamo, L., Ferrare, R., Lawson, P., Mace, G. G., Simpas, J. B., Tanelli, S., Ziemba, L., van Diedenhoven, B., Bruintjes, R., Bucholtz, A., Cairns, B., Cambaliza, M. O., Chen, G., Diskin, G. S., Flynn, J. H., Hostetler, C. A., Holz, R. E., Lang, T. J., Schmidt, K. S., Smith, G., Sorooshian, A., Thompson, E. J., Thornhill, K. L., Trepte, C., Wang, J., Woods, S., Yoon, S., Alexandrov, M., Alvarez, S., Amiot, C. G., Bennett, J. R., Brooks, M., Burton, S. P., Cayanan, E., Chen, H., Collow, A., Crosbie, E., DaSilva, A., DiGangi, J. P., Flagg, D. D., Freeman, S. W., Fu, D., Fukada, E., Hilario, M. R. A., Hong, Y., Hristova-Veleva, S. M., Kuehn, R., Kowch, R. S., Leung, G. R., Loveridge, J., Meyer, K., Miller, R. M., Montes, M. J., Moum, J. N., Nenes, T., Nesbitt, S. W., Norgren, M., Nowottnick, E. P., Rauber, R. M., Reid, E. A., Rutledge, S., Schlosser, J. S., Sekiyama, T. T., Shook, M. A., Sokolowsky, G. A., Stamnes, S. A., Tanaka,

T. Y., Wasilewski, A., Xian, P., Xiao, Q., Xu, Z., and Zavaleta, J.: The coupling between tropical meteorology, aerosol lifecycle, convection, and radiation, during the Clouds, Aerosol and Monsoon Processes Philippines Experiment (CAMP²Ex), B. Am. Meteorol. Soc., https://doi.org/10.1175/BAMS-D-21-0285.1, 2023.

Ronneberger, O., Fischer, P., and Brox, T.: U-net: Convolutional networks for biomedical image segmentation, in: International Conference on Medical image computing and computer-assisted intervention, 234–241, Springer, https://doi.org/10.1007/978-3- 319-24574-4_28, 2015.

Rothman, L., Jacquemart, D., Barbe, A., Chris Benner, D., Birk, M., Brown, L., Carleer, M., Chackerian, C., Chance, K., Coudert, L., Dana, V., Devi, V., Flaud, J.-M., Gamache, R., Gold- man, A., Hartmann, J.-M., Jucks, K., Maki, A., Mandin, J.- Y., Massie, S., Orphal, J., Perrin, A., Rinsland, C., Smith, M., Tennyson, J., Tolchenov, R., Toth, R., Vander Auwera, J., Varanasi, P., and Wagner, G.: The HITRAN 2004 molecular spectroscopic database, J. Quant. Spectrosc. Ra., 96, 139–204, https://doi.org/10.1016/j.jqsrt.2004.10.008, 2005.

Schmidt, K. S., Pilewskie, P., Platnick, S., Wind, G., Yang, P., and Wendisch, M.: Comparing irradiance fields derived from Moderate Resolution Imaging Spectroradiometer airborne simulator cirrus cloud retrievals with solar spectral flux radiometer measurements, J. Geophys. Res., 112, D24206, doi:10.1029/2007JD008711, 2007.

Schmidt, S., Pilewskie, P., Mayer, B., Wendisch, M., Kindel, B., Platnick, S., King, M. D., Wind, G., Arnold, G. T., Tian, L., Heymsfield, G., and Kalesse, H.: Apparent absorption of solar spectral irradiance in heterogeneous ice clouds, J. Geophys. Res., 115, D00J22, https://doi.org/10.1029/2009JD013124, 2010.

Song, S., Schmidt, K. S., Pilewskie, P., King, M. D., Heidinger, A. K., Walther, A., Iwabuchi, H., Wind, G., and Coddington, O. M.: The Spectral Signature of Cloud Spatial Structure in Shortwave Irradiance, Atmos. Chem. Phys., 16, 13791–13806, https://doi.org/10.5194/acp-16-13791-2016, 2016.

Strahler, A., Muller, J., Lucht, W., Schaaf, C., Tsang, T., Gao, F., Li, X., Lewis, P., and Barnsley, M.: MODIS BRDF/albedo product: algorithm theoretical basis document version 5.0, MODIS documentation, 1999.

Spada, F., Krol, M. C., and Stammes, P.: McSCIA: application of the Equivalence Theorem in a Monte Carlo radiative transfer model for spherical shell atmospheres, Atmos. Chem. Phys.,

1374   6, 4823–4842, https://doi.org/10.5194/acp-6-4823-2006, 2006.

1375 Várnai, T., A. Marshak, C.-H. Huang: Publicly available online simulator of 3D radiative

1376   processes, International Radiation Symposium 2022, Thessaloniki, Greece, 4–8 July 2022,

1377   File   listed   as   IRS_2022_paper_89.pdf   at

1378   https://mycloud.auth.gr/index.php/s/t7fYkzsiFWYFdqy?path=/S4-

1379   General_Remote_Sensing, 2022.

1380 Wood, J., Smyth, T. J., and Estellés, V.: Autonomous marine hyperspectral radiometers for

1381   determining solar irradiances and aerosol optical properties, Atmos. Meas. Tech., 10, 1723–

1382   1737, https://doi.org/10.5194/amt-10-1723-2017, 2017.

1383